Accepted to Phys. Fluids 10.1063/5.0152104

Intercomparison of hydrostatic and nonhydrostatic modeling for tsunami inundation mapping

Yefei Bai (白晔斐)[1], Yoshiki Yamazaki (山崎良樹)[2], Kwok Fai Cheung (張國輝)[2,a)]

AFFILIATIONS

[1]Ocean College, Zhejiang University, Zhoushan, Zhejiang 316021, China

[2]Department of Ocean and Resources Engineering, University of Hawaii at Manoa, Honolulu, Hawaii 96822, USA

Note: This paper is part of the special topic, Physics and Modelling of Tsunamis

[a)]Author to whom correspondence should be addressed: cheung@hawaii.edu

ABSTRACT

Nonhydrostatic modeling has emerged as an effective tool for seismological and tsunami research for over a decade, but its general application in hazard mapping and engineering design remains a topic of discussion. The approach incorporates the depth-averaged vertical velocity and nonhydrostatic pressure in the nonlinear shallow-water equations that provide a Poisson-type equation via the conservation of mass for quasi three-dimensional flows. After the 2011 Tohoku tsunami, the State of Hawaii augmented the existing inundation maps to account for probable maximum tsunamis from Mw 9.3 and 9.6 Aleutian earthquakes. The use of both hydrostatic and nonhydrostatic modeling with a common set of telescopic computational grids covering 1330 km of shorelines facilitates a thorough intercomparison under distinct extreme events over a range of tropical island terrain and bathymetry. Including vertical flow dynamics can enhance formation of a slowly attenuating trough behind the leading crest across the ocean as well as drawdown of receding water over steep nearshore slopes. The nonhydrostatic approach consistently gives lower predictions of the offshore tsunami amplitude due to frequency dispersion but can produce more severe coastal surges from resonance of the leading crest and trough over insular slopes as

well as trapping of tsunami waves over wide shelves. Despite the potential for underestimating coastal surges, the lack of vertical inertia in hydrostatic models can result in substantially larger runup over steep terrain. The tsunami processes leading to inundation are complex with a strong dependence on the waveform and topography that can be well elucidated by the nonhydrostatic approach.

I. INTRODUCTION

Tsunamis pose a constant threat to coastal communities around the world. A number of countries have implemented evacuation and design-zone maps for emergency management and infrastructure development. These data products typically reflect predicted coastal inundation in extreme tsunami scenarios associated with subduction zone earthquake or submarine landslide activities. Nonlinear shallow-water models have been a popular tool for inundation mapping due to their low computing costs, ease of implementation, and long record of applications (e.g., Imamura et al., 1988; Kowalik and Murty, 1993; Liu et al., 1995; Titov and Synolakis, 1998). Shock-capturing schemes are fully compatible with the hyperbolic governing equations for modeling of flow discontinuities and are instrumental for conservation of flow volume in mapping tsunami inundation under extreme scenarios (e.g., Wei et al., 2006; LeVeque et al., 2011). This model capability is also important for assessing potential bore formation in engineering design as the subsequent impact pressure on structures can be significantly higher and far more complex than that from a surge (e.g., Huo and Liu, 2023). The hydrostatic system, which describes flow dynamics in the horizontal directions only, caters to shallow-water waves on gradually-varying seafloor with celerity independent of the period. Although tsunami waves are weakly dispersive, the slight offset in celerity can accumulate to produce first-order effects on the waveform and amplitude in the far field.

Boussinesq-type and nonhydrostatic models provide a more refined tool to describe tsunami processes for scientific research and practical application. Their formulations augment the shallow-water approach with a leading-order approximation for weakly dispersive waves. The

Boussinseq-type equations account for vertical flow dynamics through higher-order derivatives of the horizontal velocity (e.g., Horrillo et al., 2006; Kirby et al., 2013; Baba et al., 2017), while the nonhydrostatic approach explicitly includes the depth-averaged vertical velocity and nonhydrostatic pressure in a quasi three-dimensional model (Yamazaki et al., 2009, 2011). The resulting dispersion property leads to lagging of shorter-period components and reduction of the overall wave amplitude for a more realistic depiction of tsunami propagation across the ocean (e.g., Saito et al., 2014; Bai and Cheung, 2016). Additionally, inclusion of vertical flow dynamics can improve physical representation of tsunami source processes as well as flows over steep insular and continental slopes. These higher-order properties through variant forms of governing equations also have applications in maritime and open-channel hydraulics, which have traditionally been treated as hydrostatic with shallow-water models (Castro-Orgaz et al., 2023). Both Boussinesq-type and nonhydrostatic models can include a shock-capturing scheme in spite of their dispersion property. Local disabling of higher-order terms reduces the governing equations to hyperbolic for approximation of bores or hydraulic jumps in runup and drawdown computations.

Public safety is of paramount importance whether it is for emergency management or infrastructure planning. The devastation caused by the 2011 Tohoku tsunami highlights the need to reassess and mitigate the hazards with best available information. In the aftermath, the State of Hawaii augmented the existing inundation maps with an additional zone for probable maximum tsunamis. The project required both hydrostatic and nonhydrostatic modeling for quality assurance and control between the commonly-used shallow-water approach and the newly-developed, higher-order model of Yamazaki et al. (2009, 2011) at the time. The effort was unprecedented as a practical application in emergency management as well as a test bed for emerging techniques, and most notably, answered an important question whether nonlinear shallow-water models produce more severe coastal impacts by overestimating the incident wave amplitude and thus suffice as a conservative tool for hazard mapping and engineering design. The nonhydrostatic approach has subsequently been validated by numerical and laboratory experiments as well as comprehensive observations from the 2011 Tohoku tsunami (Yamazaki et al., 2018; 2023), while garnered a track record for megathrust earthquake and tsunami research (e.g., Lay et al., 2013; Yue et al., 2014; Li et al., 2016; Ye et al., 2022; Bai et al., 2022, 2023). With increased confidence and understanding of nonhydrostatic modeling in relation to the Boussinesq-type approach (Bai et al., 2018b), we thoroughly reevaluate the data products from the earlier inundation mapping project to highlight the role of vertical flow dynamics in tsunami processes and identify potential limitations of the hydrostatic approach for flood hazard mapping.

II. NONHYDROSTATIC MODEL

The nonhydrostatic model of Yamazaki et al. (2009, 2011) is known as NEOWAVE (Non-hydrostatic Evolution of Ocean WAVEs) with users in the tsunami and seismological research communities around the world (e.g., Romano et al., 2012; Aránguiz et al., 2014; Bletery et al., 2014; Catalán et al., 2015; Salazar et al., 2022). NEOWAVE has been benchmarked with laboratory and field datasets under the auspices of the US National Tsunami Hazard Mitigation Program for flood and maritime hazard mapping (Yamazaki et al., 2012; Bai et al., 2015). The modular code structure, which is inherent in the governing equations and numerical schemes, allows assembly of model functionalities for requirement-specific applications. An understanding of the basic mathematical and numerical formulations along with their intrinsic properties is essential for implementation of the model as well as interpretation of the hydrostatic and nonhydrostatic solutions.

A. Mathematical Formulation

The depth-integrated Euler equations of Stelling and Zijlema (2003) are extended to include seafloor displacement η and a spherical coordinate system (λ, ϕ, z) for tsunami modeling. Fig. 1 provides a schematic of the mathematical model for nonhydrostatic free-surface flows. The sea-surface elevation ζ and water depth h are measured from the still-water level at $z = 0$. The depth-averaged horizontal velocity (U, V) defines the flow field in the λ and ϕ directions as in the shallow-water approach. With t denoting time and R the earth radius, the kinematic free-surface and seabed boundary conditions provide the vertical velocity

$$w_s = \frac{\partial \zeta}{\partial t} + \frac{U}{R\cos\phi}\frac{\partial \zeta}{\partial \lambda} + \frac{V}{R}\frac{\partial \zeta}{\partial \phi} \qquad \text{at } z = \zeta \tag{1}$$

$$w_b = \frac{\partial \eta}{\partial t} - \frac{U}{R\cos\phi}\frac{\partial (h-\eta)}{\partial \lambda} - \frac{V}{R}\frac{\partial (h-\eta)}{\partial \phi} \quad \text{at } z = -h + \eta \tag{2}$$

A linear profile gives the depth-averaged vertical velocity $W = (w_s + w_b)/2$ consistent with long-wave theory. Let Ω, g, ρ, and n denote the earth angular velocity, gravitational acceleration, water density, and Manning's number. The continuity and λ, ϕ, and z-momentum equations read

$$\frac{\partial(\zeta-\eta)}{\partial t} + \frac{1}{R\cos\phi}\frac{\partial(UD)}{\partial\lambda} + \frac{1}{R\cos\phi}\frac{\partial(VD\cos\phi)}{\partial\phi} = 0 \tag{3}$$

$$\begin{aligned}&\frac{\partial U}{\partial t} + \frac{U}{R\cos\phi}\frac{\partial U}{\partial\lambda} + \frac{V}{R}\frac{\partial U}{\partial\phi} - \left(2\Omega + \frac{U}{R\cos\phi}\right)V\sin\phi \\ &= -\frac{g}{R\cos\phi}\frac{\partial\zeta}{\partial\lambda} - \frac{1}{\rho R\cos\phi}\frac{\partial Q}{\partial\lambda} - \frac{Q}{\rho DR\cos\phi}\frac{\partial(\zeta-h+\eta)}{\partial\lambda} - n^2\frac{g}{D^{1/3}}\frac{U\sqrt{U^2+V^2}}{D}\end{aligned} \tag{4}$$

$$\begin{aligned}&\frac{\partial V}{\partial t} + \frac{U}{R\cos\phi}\frac{\partial V}{\partial\lambda} + \frac{V}{R}\frac{\partial V}{\partial\phi} - \left(2\Omega + \frac{U}{R\cos\phi}\right)U\sin\phi \\ &= -\frac{g}{R}\frac{\partial\zeta}{\partial\lambda} - \frac{1}{\rho R}\frac{\partial Q}{\partial\phi} - \frac{Q}{\rho DR}\frac{\partial(\zeta-h+\eta)}{\partial\phi} - n^2\frac{g}{D^{1/3}}\frac{V\sqrt{U^2+V^2}}{D}\end{aligned} \tag{5}$$

$$\frac{\partial W}{\partial t} = \frac{2Q}{\rho D} \tag{6}$$

where $D = h + \zeta - \eta$ is the flow depth and Q is the depth-averaged non-hydrostatic pressure with an assumed linear profile diminishing to zero at $z = \zeta$ to satisfy the dynamic free-surface boundary condition. The z momentum equation balances the vertical flow inertia with the nonhydrostatic pressure, which in turn constitutes a forcing mechanism of the flow in the λ and ϕ directions. Its nonlinear advective terms are small for long waves and thus have been omitted in Eq. (6) for model simplicity. The governing equations involve first-order temporal and spatial derivatives, but implicitly include higher-order properties comparable to the Boussinesq-type approach.

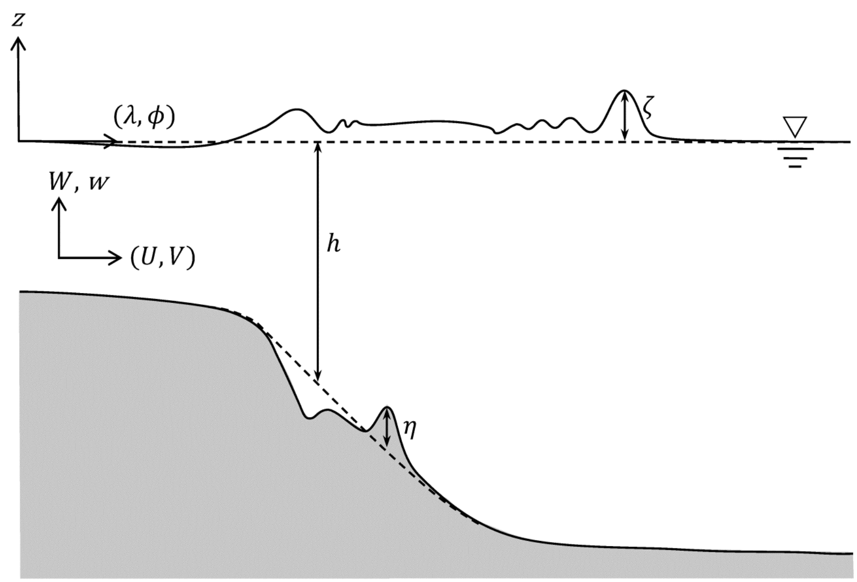

FIG. 1. Schematic of mathematical model.

The spherical coordinate system (λ, ϕ, z) reduces to the Cartesian system (x, y, z) for mathematical analysis of the governing equations. After dropping the nonlinear and seafloor displacement terms, substitution of a system of periodic waves with amplitude A and wave number k yields the dispersion relation for a uniform depth h. This provides the celerity of the nonhydrostatic model as

$$c_{Nh} = \sqrt{gh}\left[1 + \frac{1}{4}(kh)^2\right]^{-1/2} \tag{7}$$

where kh is the depth parameter. Eq. (7) has the same form as the dispersion relation derived from the Boussinesq-type equations of Peregrine (1967), but with a coefficient of 1/4 instead of 1/3 for the $(kh)^2$ term resulting in slight underestimation of dispersion effects for $kh < 2.4$ in comparison to Airy wave theory. This is attributed to the approximation of the vertical velocity and nonhydrostatic pressure with linear profiles in the mathematical model (Bai et al., 2018b). Full compatibility with Peregrine (1967), which gives accurate dispersion within the typical tsunami range of $kh < 0.6$, can only be achieved by a quadratic profile of the nonhydrostatic pressure (Jeschke et al., 2017). For a sloping bottom, A and k are functions of x giving the linear shoaling gradient defined by Madsen and Sørensen (1992) for the nonhydrostatic model as

$$\begin{aligned}\gamma_{Nh} &= -\frac{h}{A}\frac{\partial A}{\partial x}\Big/\frac{\partial h}{\partial x} \\ &= \frac{1}{4} - \frac{3}{16}(kh)^2\end{aligned} \tag{8}$$

which matches well with Airy wave theory with parallel or better performance compared to Peregrine (1967) up to kh = 1.2 (Bai et al., 2018b). Both the celerity and shoaling gradient are functions of kh to better resolve wave propagation across the ocean and transformation over continental and insular slopes. These higher-order processes can modulate the spectral content and phase as tsunami waves de-shoal over the continental slope at the source and reverse the processes prior to impacting a coastline. Under hydrostatic conditions, the vertical velocity and nonhydrostatic pressure vanish and the governing system in Eqs. (3) - (6) reduces to the nonlinear shallow-water equations. The celerity and shoaling gradient in Eqs. (7) and (8) become $c_H = \sqrt{gh}$ and $\gamma_H = 1/4$ independent of the depth parameter.

B. Numerical Formulation

The fractional-step method provides the nonhydrostatic solution over a staggered finite-difference grid at each time step. The spatial derivatives are computed by second-order central differences and the flux terms by the first-order upwind scheme of Mader (2004), which extrapolates ζ instead of the flow depth D as typically done. The resulting advective speed is implemented with the shock-capturing method of Stelling and Duinmeijer (2003) for modeling of discontinuous flows. Time integration of the momentum equations (4) - (6) provides the depth-averaged horizontal velocity (U, V) and vertical velocity $W = (w_s + w_b)/2$ in terms of the nonhydrostatic pressure Q for substitution into the conservation of mass

$$\frac{1}{R\cos\phi}\frac{\partial U}{\partial\lambda} + \frac{1}{R\cos\phi}\frac{\partial(V\cos\phi)}{\partial\phi} + \frac{\partial w}{\partial z} = 0 \tag{9}$$

in which $\partial w/\partial z = (w_s - w_b)/D$ for the linear velocity profile in the long-wave approximation. This leads to a Poisson-type equation to determine Q for update of (U, V) and ζ before advancing to the next time step. Grid refinement is embedded in the time integration to model multi-scale processes. Nesting schemes typically interpolate the flux (*UD*, *VD*) in time and space for input to a finer, inner grid and average the resulting ζ as feedback to the outer grid (e.g., Imamura et al., 1988; Liu et al., 1995). The present model also inputs ζ and Q to facilitate propagation of shock and dispersive waves across inter-grid boundaries. The dispersion terms with first-order spatial derivatives enable implementation of the Dirichlet condition to ensure continuity of the nonhydrostatic solution. The two-way inter-grid data transfer is accurate and robust with validated results for grid refinement ratios up to 10 at the rugged shorelines of Hawaii (e.g., Cheung et al., 2013; Lay et al., 2013; Yamazaki et al., 2023). A flexible indexing system enables adaptation of inter-grid boundaries to topographic features for optimal resolution and computational efficiency.

The finite-difference schemes introduce truncation errors that interfere with the dispersion property of the governing equations. Li and Cheung (2019) derived the dispersion relation for NEOWAVE in the Cartesian coordinate system (x, y) that includes the spatial discretization (Δx, Δy) and time step Δt. For illustration with wave propagation along the x axis, a Taylor series expansion of the dispersion relation gives a leading-order approximation of the celerity as

$$c_{Nh,\Delta^2} = \sqrt{gh}\left\{\frac{1+\left[\frac{1}{4}-\frac{\alpha}{12}\right](kh)^2-\frac{\alpha}{24(1-Cr^2)}(kh)^4}{1+\frac{1}{2}(kh)^2+\left[\frac{1}{16}-\frac{\alpha}{24(1-Cr^2)}\right](kh)^4-\frac{\alpha}{96(1-Cr^2)}(kh)^6}\right\}^{1/2} \quad (10)$$

where $Cr = \sqrt{gh}\Delta t/\Delta x$ is the Courant number and $\alpha = (\Delta x^2 - gh\Delta t^2)/h^2$ combines the effects of grid size, time step, and water depth to indicate the level of numerical dispersion relative to the intrinsic property from the governing equations. A comparison between Eqs. (7) and (10) shows the discretization augments the dispersion relation from a [0, 2] to a [4, 6] rational function. A value of $\alpha = 0.8$ provides the optimal numerical dispersion to complement the underestimated, intrinsic property from the governing equations in matching Airy wave theory up to $kh = 1.2$. The Boussinesq-type equations, which provide asymptotic convergence of nonhydrostatic properties, inevitably lead to excess dispersion in tsunami modeling as reported by Baba et al. (2017). Similarly, the hydrostatic model gives the celerity as

$$c_{H,\Delta^2} = \sqrt{gh}\left[1 - \frac{\alpha}{12}(kh)^2\right]^{1/2} \tag{11}$$

in which a value of $\alpha = 4$ recovers the leading-order term of the dispersion relation from the Boussinesq-type equations of Peregrine (1967). In lieu of dispersion from the governing equations, the celerity is still a function of kh through the discretization parameter α.

The depth-integrated formulation describes breaking waves as bores or hydraulic jumps through momentum conservation within the staggered grid system and accounts for energy dissipation across flow discontinuities without predefined mechanisms or empirical coefficients. The nonhydrostatic governing equations, however, counteract these shock-related hydraulic processes from the numerical scheme with frequency dispersion (Roeber and Cheung, 2012). The artifacts are generally minor, but might cause numerical instability for energetic breaking waves with discontinuities comparable to the grid size. In circumventing the internal model confliction, NEOWAVE switches off the nonhydrostatic terms according to the breaking initiation and cessation criteria

$$\frac{\sqrt{U^2+V^2}}{\sqrt{gD}} > 0.5 \text{ and } < 0.15 \tag{12}$$

which were determined from a series of laboratory benchmarks (Yamazaki et al., 2012). The governing equations (3) - (6) locally reduce to the nonlinear shallow-water equations for bore or hydraulic jump formation in the nearshore region. The subsequent runup and drawdown from flood and ebb flows are primarily hydrostatic. The computational grid differentiates wet and dry cells by the flow depth D and sets the nonhydrostatic pressure to zero along the interface for improved stability. The time integration scheme tracks any advancement of the wet-dry interface through extrapolation of (U, V) and ζ from the wet to dry cells. This approach works well with the first-order upwind scheme of Mader (2004) in minimizing extrapolation errors over irregular coastal reef and terrain in tropical island environments.

III. TSUNAMI INUNDATION MAPPING

Hawaii is the first state in the US to enforce coastal evacuation during tsunami warnings. The delineation of evacuation zones involves administrative, logistic, and social constraints, but always relied on inferred inundation with a reasonable chance of occurring. Cox (1961) developed the first statewide tsunami inundation maps from recorded runup of the 1946 Aleutian, 1952 Kamchatka, 1957 Aleutian, and 1960 Chile tsunamis, which had been the most destructive in the prior 142 years of Hawaii's written history. Subsequent updates included the 1964 Alaska tsunami with runup exceeding some of the previous observations on east and north-facing shores (Walker, 2004). The 2011 Tohoku tsunami, which devastated northeast Japan, led to development of extreme inundation scenarios beyond what can be inferred from historical records. Prior updates of the inundation maps were based on nonlinear shallow-water models, in which the lack of higher-order properties had motivated the development of NEOWAVE for the tropical volcanic island environment of Hawaii. The project called for both hydrostatic and nonhydrostatic modeling for all shorelines with at-risk population and infrastructure to cross-reference the data products in developing the official inundation maps for the state. The modular code structure allows computations in either mode using the same tsunami excitation and model setting for direct comparison of the results.

A. Earthquake and Tsunami Excitation

The tsunami generated by the 2011 Mw 9.0 Tohoku earthquake did not exceed Hawaii's evacuation maps, but prompted a reexamination of the earthquake scenarios for hazard mapping. Studies of the well-recorded event provided timely information on the earthquake source as well as insights into the near and far-field wave dynamics (e.g., Fijiwara et al., 2011; Yamazaki et al., 2011, 2013; Cheung et al., 2013). Some of the most striking aspects are the large slip of more than 50 m near the Japan Trench and the susceptibility of near-shore waters to undergo resonance oscillations around the Pacific. In Hawaii, persistent surges and strong currents led to closure of harbors and marinas for up to 38 hours after wave arrival. The dominant modes around the Hawaiian Islands range from 11 to 75 min across the full spectrum of tsunami waves (Figs. A1 and A2). These factors strongly influenced the development and selection of earthquake sources for the inundation map update. Of the five historical tsunami sources used in the existing maps at the time, four have estimated moment magnitude greater than 9.2, whereas the 1946 Aleutian earthquake has lower magnitude of 8.6. Although the 1946 event is known to be a tsunami earthquake with a disproportionate tsunami for the earthquake magnitude (Kanamori, 1972), preliminary assessment showed tsunamis generated by Aleutian earthquakes of approximately Mw 9.0 would likely exceed the evacuation map based on the five historical events.

Butler (2012, 2014) reexamined the potential for great earthquakes along the Aleutian island arc and the work led to development of two scenarios with Mw 9.3 and 9.6 for the inundation mapping effort. The proposed scenarios are reminiscent of largest earthquakes on record around the world and are within the plausible range of Mw 9.20 to 9.63 for the Aleutian-Alaska subduction zone agreed by an international team of seismologists in the aftermath of the 2011 Tohoku earthquake (Berryman *et al*., 2013). The Mw 9.3 and 9.6 earthquakes rupture 700 and 1400 km of the megathrust fault with the same average slip of 35 m, which was inferred from the strongest instrumentally recorded, 1960 Mw 9.5 Chile earthquake. The current convergence rate of 7 cm/year and the preferred coupling coefficient of 0.5 from Berryman *et al*. (2013) suggest 1000 years of accumulated strain for the 35 m average slip in the subduction zone. Paleotsunami deposits at eastern Aleutian sites suggest recurrence of large earthquakes between 164 and 257 years in the last 2000 years (Witter et al., 2016; 2018). One inferred event overlaps the radiocarbon-dated age of tsunami deposits at three Hawaii sites between 500 to 700 calibrated years before the present (La Selle et al., 2020). There is no conclusive evidence of other tsunami deposits at the three Hawaii sites until the 1946 and 1957 Aleutian tsunamis. The Mw 9.3 and 9.6 events thus have very low probability of occurrence in light of these recent findings, but given the unexpected 2011 Tohoku earthquake and tsunami, serve as conservative scenarios for evacuation planning. The large earthquake magnitudes and locations directly due north provide the probable maximum tsunami scenarios for Hawaii.

Fig. 2 illustrates the fault slip and earth-surface deformation for the two great Aleutian earthquake scenarios. Each subfault is 50 by 100 km in dip and strike with tectonic parameters from Gica et al. (2008). The Mw 9.3 earthquake has a uniform fault width of 100 km along its 700-km length. The rupture extends 50 km down dip with 50 m slip and has a smaller value of 20 m in the deeper 50-km segment. The non-uniform slip shifts the crustal deformation toward the trench to enhance the tsunami excitation in mimicking the 2011 Tohoku earthquake (Lay, 2018). In contrast, the Mw 9.6 event is a scale-up version of the 2004 Sumatra-Andaman earthquake (Ammon et al., 2005; Lay et al., 2005). The faulting involves uniform slip of 35 m and variable widths of 100 and 150 km along its 1400-km length. Such occurrence has an even lower probability than the Mw 9.3 event due to rupture across multiple fault segments along the Alaska Peninsula, where recent geodetic data and earthquakes indicate varying, low coupling in the down-dip megathrust with patchy locked zones as well as event-driven rapid afterslip in the up-dip region (e.g., Li and Freymueller, 2018; Ye et al., 2022; Bai et al., 2022; Brooks et al., 2023), but nonetheless, provides another extreme end member for evaluation of tsunami modeling techniques. The planar fault model of Okada (1985) defines the elastic crustal deformation with uplift and subsidence reaching 21.8 and 4.6 m for the Mw 9.3 earthquake and 15.7 and 8.2 m for the Mw 9.6 event. The rupture is modeled as instantaneous with the same seafloor and initial sea-surface displacement to provide the same source mechanism for hydrostatic and nonhydrostatic modeling. The two great Aleutian events represent a range of catastrophic earthquakes and the resulting tsunamis cover a broad spectrum to excite the oscillation modes in Hawaii waters.

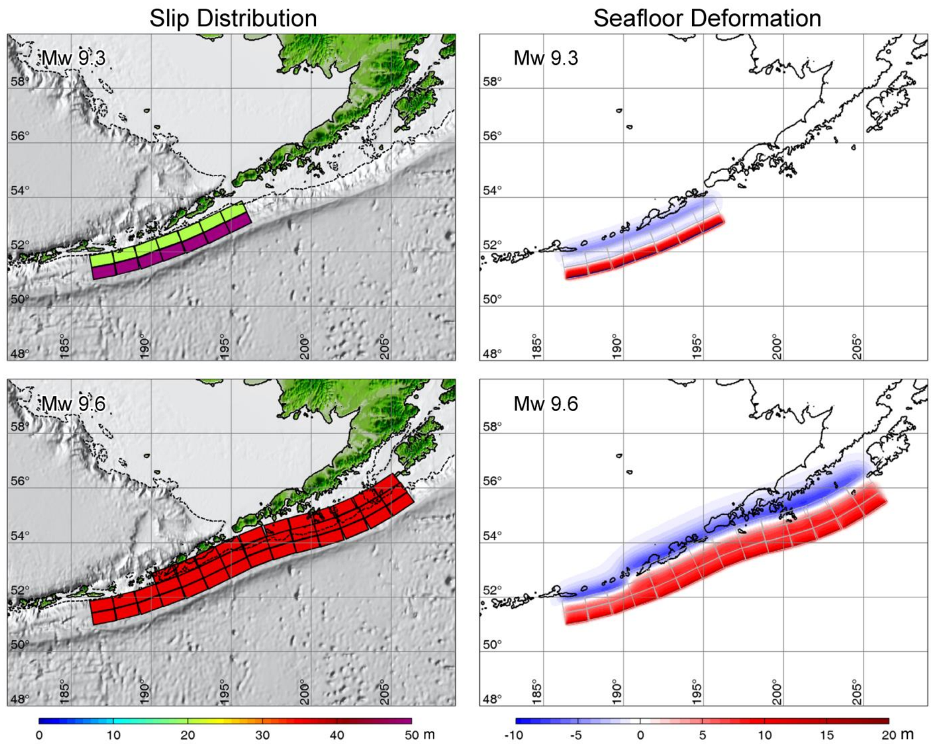

FIG. 2. Slip distribution and seafloor deformation for Mw 9.3 and 9.6 Aleutian earthquakes derived from Butler (2012) and Butler et al. (2014). Dashed lines in left panels are 200-m depth contours indicating the approximate extent of the continental shelf.

B. Model Setup

The modeling requires up to five levels of two-way nested computational grids to describe tsunami processes with increasing resolution from the open ocean to the shore. The digital elevation model includes ETOPO1 published by the US National Geophysical Data Center in 2009, gridded multi-beam data around the Hawaiian Islands at 1.5 arcsec (~45 m) released by the University of Hawaii in 2007 as well as coastal LIDAR bathymetry and topography of Hawaii at 1~3 m resolution collected by US Army Corps of Engineering between 1999 and 2009. Fig. 3 illustrates the model setup through the telescopic grid system for inundation mapping at Haleiwa, Oahu. The level-1 grid describes tsunami propagation from the Aleutian source to Hawaii. The 2 arcmin (~3600 m) resolution provides adequate depiction of large-scale seafloor features as well as optimal model dispersion for NEOWAVE. The level-2 grid extends along the major Hawaiian Islands at 24 arcsec (~720 m) resolution to capture inter-island standing waves (Fig. A1a). There are four level-3 grids to resolve the insular slopes and shelves for modeling of coastal trapped waves (Figs. A1b and A2). The volcanic island bathymetry is rather discontinuous. The insular shelves at 100 m depth drop off to a lower shelf at 1000 m or the abyssal seafloor at 4000-5000 m depth. Table 1 summarizes the subsequent grid refinement scheme, which varies among the islands. The 3-arcsec (~90-m) Oahu grid provides a transition to 15 level-4 grids covering the entire shoreline at 0.3 arcsec (~9 m) resolution. The nearshore bathymetry is complex with coastal reefs extending from the shore to ~20 m water depth followed by a steep drop-off of the limestone substrate to ~30 m and a second drop-off at ~50 m depth (Fletcher and Sherman, 1995). Fringing reefs, channels, coastal dunes, subdivisions, and highway embankments at Haleiwa are clearly discernible and are fully accounted for in the inundation computation.

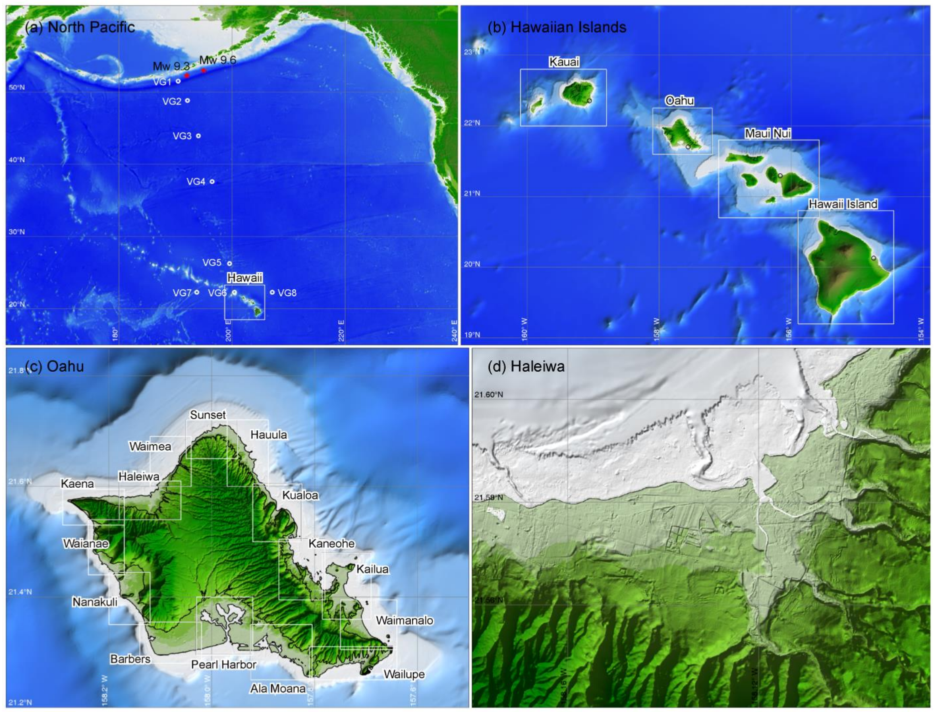

FIG. 3. Location maps, digital elevation models, and layout of telescopic computational grid system for inundation modeling at Haleiwa, Oahu. (a) Level-1 north Pacific grid with outline of level-2 Hawaii grid. Red stars indicate earthquake centriod locations and circles denote waypoints for signal comparison. (b) Level-2 Hawaii grid with outlines of level-3 Kauai, Oahu, Maui Nui, and Hawaii Island grids. Circles indicate tide gauge locations, where the MHHW defines the initial water levels for inundation modeling within the respective level-3 grids. (c) Level-3 Oahu grid with outlines of level-4 grids and the 50-m elevation contour indicating transition to mountainous terrain. (d) Level-4 grid at Haleiwa.

TABLE 1. Grid refinement scheme from levels 3 to 5.

	Level 3	Level 4	Level 5
Niihau	3 arcsec (~90 m)	-	-
Kauai	3 arcsec (~90 m)	0.3 arcsec (~9 m)*	-
Oahu	3 arcsec (~90 m)	0.3 arcsec (~9 m)	-
Maui Nui	3 arcsec (~90 m)	0.3 arcsec (~9 m)	-
Hawaii Island	6 arcsec (~180 m)	3-arcsec (~90 m)	0.3 arcsec (~9 m)

*Target resolution

The neighbor islands are sparsely populated and selected shorelines are modeled at high resolution for inundation mapping. Fig. 4 shows the level-3 grids, the layout of level-4 and 5 grids, and examples of level-4 or 5 grids to illustrate the diverse terrain. The level-3 Kauai grid includes Niihau at 90-m resolution to capture the coupled edge waves between the two islands. Inundation is mapped at a target resolution of 9 m along the rugged shoreline of Kauai. The level-4 Hanalei grid on the north shore shows complex terrain including steep cliffs and terraces, flat coastal plains, and narrow alluvial valleys that provides a critical test for model stability in terms of grid resolution. Maui, Molokai, Lanai, and Kahoolawe, which are geologically known as Maui Nui for their interconnected insular shelves and slopes, are covered by a single level-3 grid at 90-m resolution. Approximately 70% of the shorelines are modeled at 9 m resolution for inundation mapping. The level-4 Kahului grid resolves the harbor breakwaters and fringing reefs within the basin to a high level of detail. Hawaii Island, which has the largest landmass, requires an additional level of grids for computational efficiency. The level-3 grid resolves the steep insular slope around the island at a lower resolution of 180 m. Five level-4 grids at 90 m resolution provides transition to sixteen 9-m level-5 grids along the shore. The level-5 Hilo grid shows a breakwater atop of a wide reef flat and a harbor basin dredged from the reef system in a V-shape embayment known for tsunami excitation.

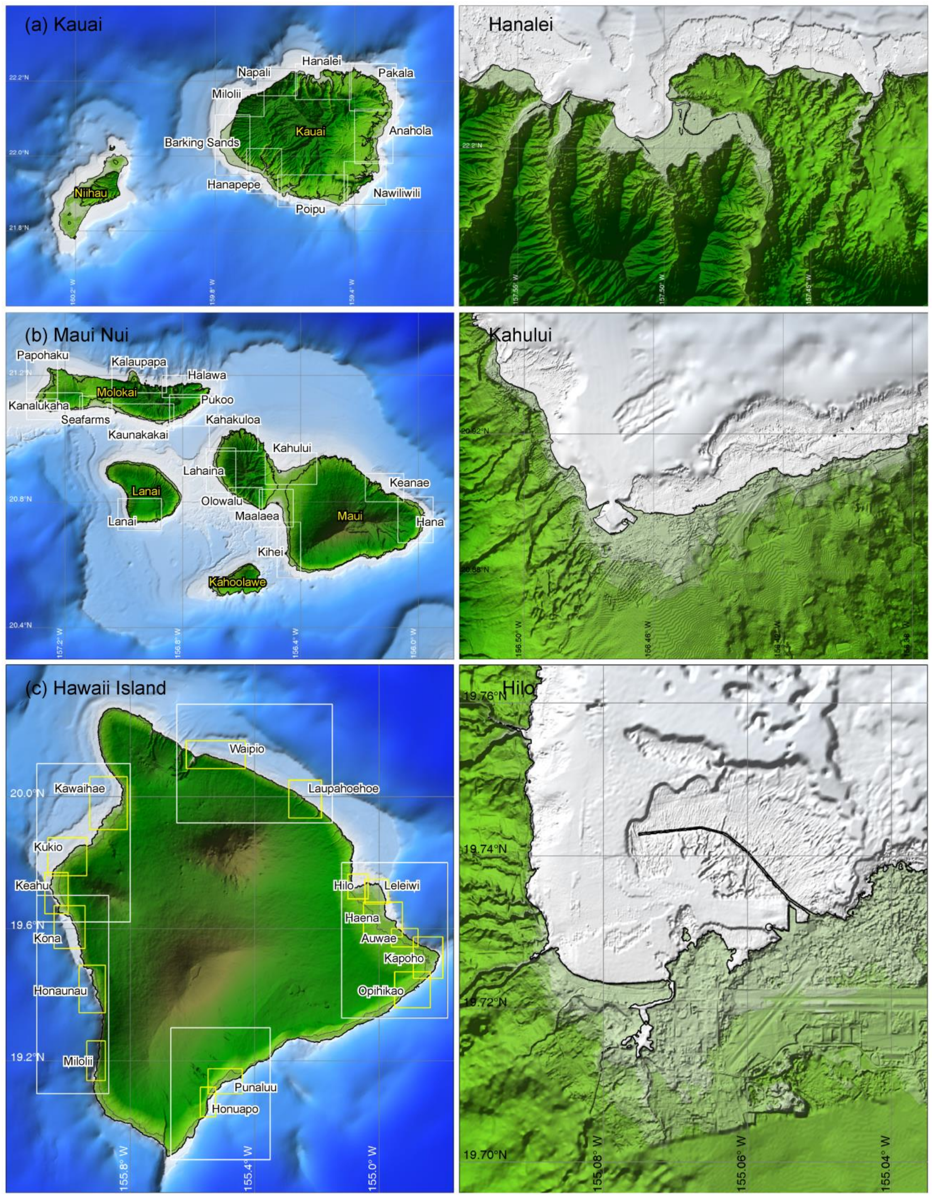

FIG. 4. Location maps, digital elevation models, and layout of telescopic computational grid systems for neighbor islands. (a) Level-3 Kauai grid with outlines of level-4 grids and Hanalei as an example. (b) Level-3 Maui Nui grid with outlines of level-4 grids and Kahului as an example.

(c) Level-3 Hawaii Island grid with outlines of level-4 and 5 grids and Hilo as an example. White and yellow rectangles indicate level-4 and 5 grids. The level-3 grids also show the 50-m elevation contours indicating transition to mountainous terrain. Circles in the Kahului and Hilo high-resolution grids indicate tide gauge locations within harbor basins.

The series of telescopic grid systems cover 1330 km of the 2000-km Hawaii shorelines with 56 high-resolution grids for hydrostatic and nonhydrostatic modeling of tsunami inundation. The primary factors deciding the coverage of each grid are computational requirements, expected inundation, and prominent bathymetric and topographic features, such as embayments, headlands, reefs, and channels, which influence stability of the two-way grid nesting. The slight overlap between adjacent high-resolution grids ensures that effects of inter-grid boundaries can be identified and excluded from the data products. Most of the shorelines are characterized by well-developed coastal plains with abrupt transition to mountainous terrain. The use of bare-earth LIDAR topography is consistent with standard practice for inundation mapping as specified by the US National Tsunami Hazard Mitigation Program. A Manning coefficient of 0.035 describes the subgrid roughness for the volcanic and reef substrates of the Hawaiian Islands (Bretschneider et al., 1986). The local mean-sea level is the datum of the digital elevation model and the reference for water depths, sea-surface elevations, and runup heights reported in this study. The tide range is around 0.6 m and the mean-higher-high-water levels at the Nawiliwili, Honolulu, Kahului, and Hilo tide gauges define the initial conditions for inundation modeling at Kauai, Oahu, Maui Nui, and Hawaii Island shores respectively (see Fig. 3b for location). Freshwater discharges from rivers and streams are minor and not considered in the modeling. With a tsunami travel time of 4.5 hours from the Aleutian Islands, the computation covers 8.5 hours of elapsed time from earthquake initiation. This allows development of interisland and shelf standing waves as well as gradual buildup of floodwater on flat coastal plains to reach the inundation limit.

IV. RESULTS AND DISCUSSION

The hydrostatic and nonhydrostatic modeling of the Mw 9.3 and 9.6 Aleutian tsunami scenarios produced a large volume of spatiotemporal data for post-processing and analysis. The dataset includes sea-surface elevation at 1-min intervals and its run-time aggregated maximum over the entire systems of telescopic grids. The computation is generally stable with minimal adjustment of the gridded topography and bathymetry, but for the level-4 Hanalei grid, coarser 0.5 and 0.75 arcsec (~15 and 22 m) resolutions, instead of the target 0.3 arcsec (~9 m), become necessary to obtain the hydrostatic and nonhydrostatic solutions for the Mw 9.3 event, which generates strong resonance responses at the north shore of Kauai. Otherwise, all inundation computations were performed with the 0.3-arcsec (~9 m) grids as summarized in Table 1. The model results are of good quality free of spurious oscillations or noticeable spikes. The absence of large seamounts along the main tsunami path allows a closer examination of frequency dispersion with minor interference from nonlinear wave scattering. The two diverse scenarios along with the wide range of tropical volcanic island terrain provide a valuable dataset for a comprehensive study of tsunami wave dynamics and inundation processes in relation to model approximation. The nonhydrostatic model, which includes quasi three-dimensional flow structures, can precisely describe tsunami processes over a wider range of scales (Yamazaki et al., 2018; 2023). The data products serve as a benchmark for evaluation of the conventional hydrostatic approach and highlighting the added values in nonhydrostatic modeling.

A. Wave Propagation and Dispersion

The Mw 9.3 Aleutian earthquake produces a skewed uplift patch over the lower continental slope with subsidence mostly on the shallow continental shelf (Fig. 2). The seafloor deformation defines the initial condition for both hydrostatic and nonhydrostatic modeling of the tsunami. Fig. 5 provides time series and spectra of the sea-surface elevation at waypoints between the source and Hawaii (see Fig. 3a for location). VG1 at the source shows descent of the initial sea-surface uplift and subsequent oscillations from leakage of trapped waves over the continental shelf. The initial sea-surface uplift comprises a series of spatial harmonics and its descent over the continental slope generates a prominent leading crest in the offshore direction with overlapping and trailing pulses. The nonhydrostatic solution shows rapid separation of the harmonics and emergence of a prominent *N*-wave at VG3. The leading crest gradually loses amplitude due to frequency dispersion, while the trough maintains its depth across the ocean and subsequently amplifies over the steep insular slope of Kauai at VG6. The hydrostatic solution shows delayed separation of the harmonics by numerical dispersion alone and shorter-period trailing waves due to celerity overestimation at the source. The signals to the west at VG7 illustrate effects of nonlinear scattering by seamounts and atolls along the Northwest Hawaiian Islands. Both approaches show transformation of the incident *N*-wave into a wave train with notable transfer of energy to super-harmonics. The comparison at VG8 to the east of the island chain provides a clear contrast between the dispersive and non-dispersive waveforms after a long distance of propagation across the open ocean.

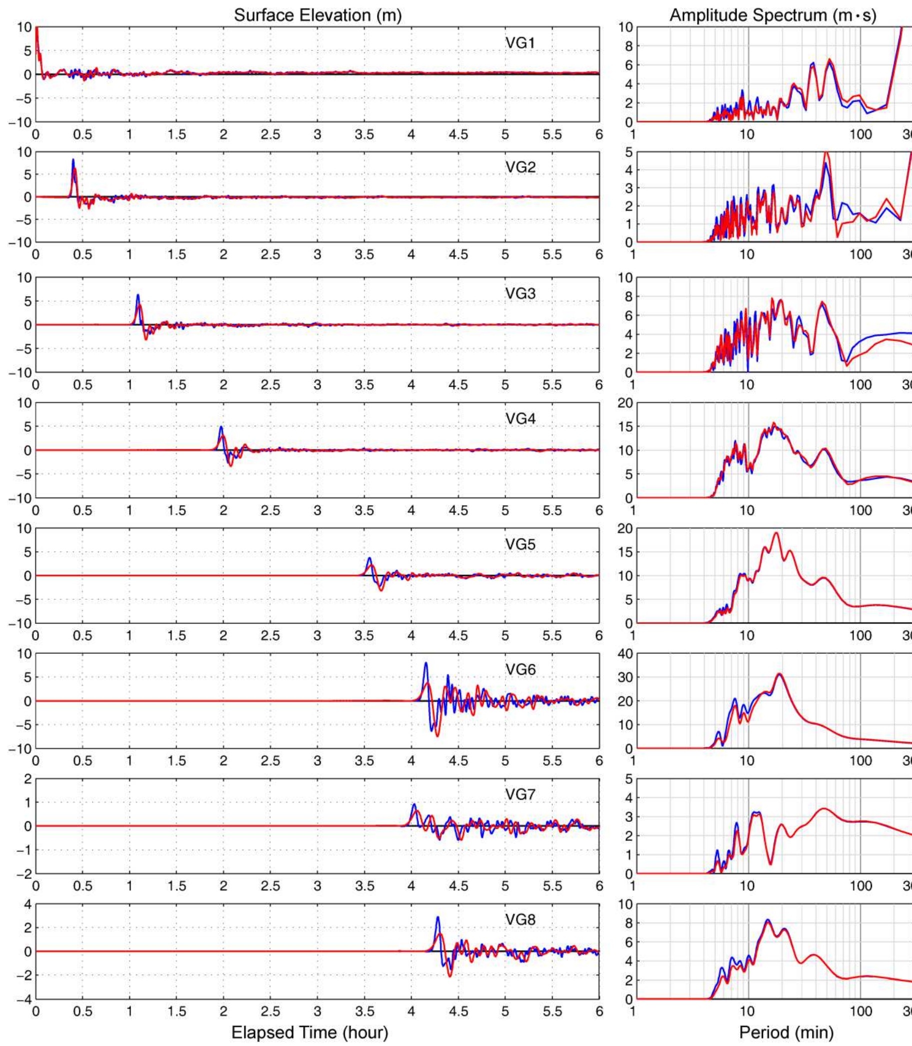

FIG. 5. Tsunami waveforms and spectra at waypoints across the North Pacific for the Mw 9.3 Aleutian earthquake (see Fig. 3a for location). Blue and red lines indicate results from hydrostatic and nonhydrostatic modeling.

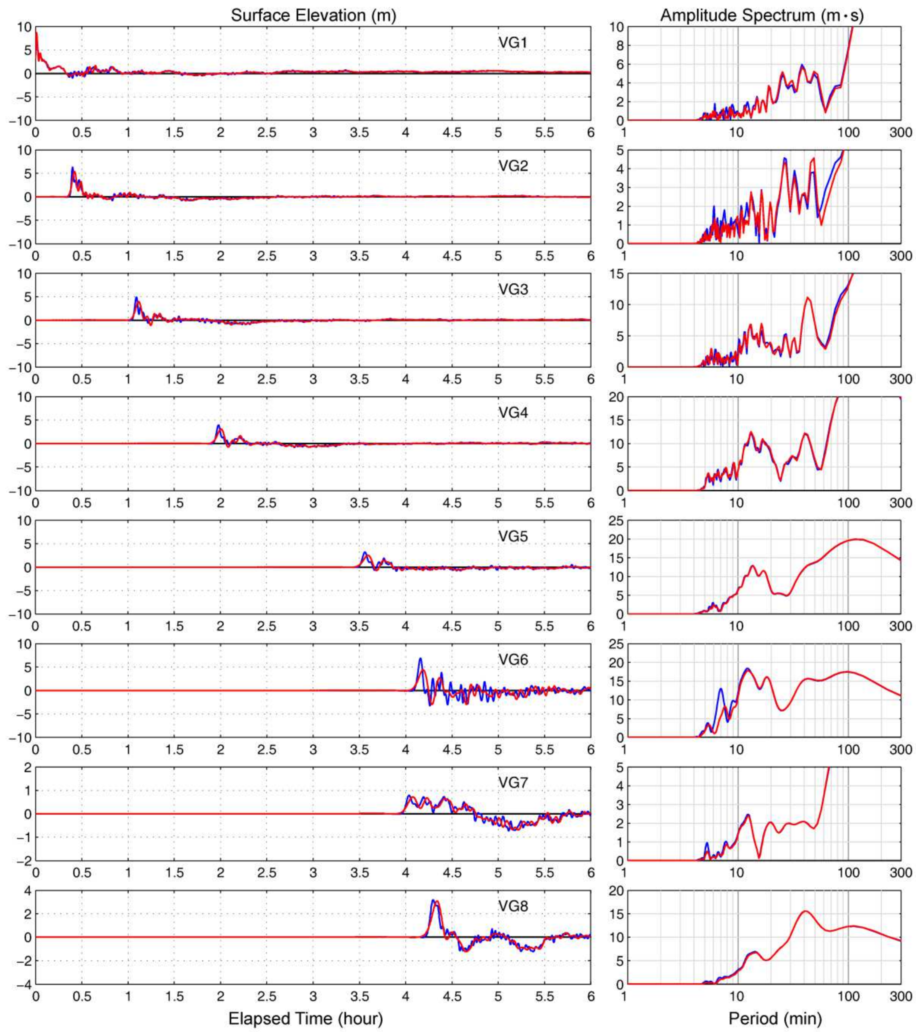

FIG. 6. Tsunami waveforms and spectra at waypoints across the North Pacific for the Mw 9.6 Aleutian earthquake (see Fig. 3a for location). Blue and red lines indicate results from hydrostatic and nonhydrostatic modeling.

The Mw 9.6 earthquake has an uplift patch extending onto the continental shelf that generates a unique tsunami as shown at the waypoints in Fig. 6. The descent of the initial sea-surface uplift produces a series of pulses due to large celerity variation across the continental margin. A pair of overlapping leading crests gradually emerges and becomes evident at VG3. Despite the large rupture area, frequency dispersion still plays a role in reducing the leading crest amplitude and separating the primary harmonics from small-amplitude, short-period waves. The hydrostatic and nonhydrostatic solutions have similar primary waveforms across the open ocean, but notably different transformation processes over the insular shelf at VG6. For both the Mw 9.3 and 9.6 events, the two approaches produce nearly identical amplitude spectra from VG3 to VG5. This demonstrates the time-averaged spectral content remains largely unaltered by dispersion and the waveform variation during propagation is due to the resulting phase shift. The hydrostatic approach results in a disproportionate increase of short-period energy at VG6 over the insular slope due to the constant shoaling gradient. The comparison provides a succinct illustration of Eq. (8), which shows a quadratic reduction of the shoaling gradient with kh, when vertical flow dynamics are included in the model. The hydrostatic approach also overestimates the short-period energy at VG7 from nonlinear scattering of the incident waves with minor effects also seen at VG8. These superharmonics are noticeable shorter compared to the dispersive waves from nonhydrostatic modeling and are typically outside the range of shelf oscillation modes to produce energetic responses around the Hawaiian Islands.

Fig. 7 provides snapshots of the sea-surface elevation immediately before arrival of the tsunamis at Hawaii. The concentrated near-trench slip in the Mw 9.3 event has the most prominent effects near the wave front, where direct radiation of the initial sea-surface uplift over the continental slope prevails. The hydrostatic solution maintains a distinct leading crest followed immediately by short-period noise within the main lobe. Dispersion in the nonhydrostatic solution produces a smaller leading crest, which is followed by a prominent trough and dispersive waves. The deep trough is associated with the large near-trench uplift of the sea surface and the subsequent downswing below the mean-water level driven by vertical flow inertia at the source. The 1946 and 1957 Aleutian tsunamis, which severely impacted Hawaii, also had a prominent trough behind the leading crest as recorded by local tide gauges (Green, 1946; Fraser et al., 1959). The uniform slip over a larger rupture area in the Mw 9.6

event results in reduced effects from vertical flow inertia at the source. The hydrostatic and nonhydrostatic approaches give closer predictions of the leading crest followed by a shallow trough north of Hawaii. The dispersive waves from the nonhydrostatic solution are longer and become more distinct in the side lobe to the east. Both the Mw 9.3 and 9.6 events have a very similar wave pattern across the ocean from leakage of trapped waves with periods ~45 min or longer over the wide continental shelf along the Alaska Peninsula. These long-period waves, which are generated by shelf resonance independent of the excitation, were also observed by an array of DART stations off the Aleutian-Alaska trench in the tsunami generated by the much smaller 2020 Mw 7.8 Simeonof earthquake (Bai et al., 2022).

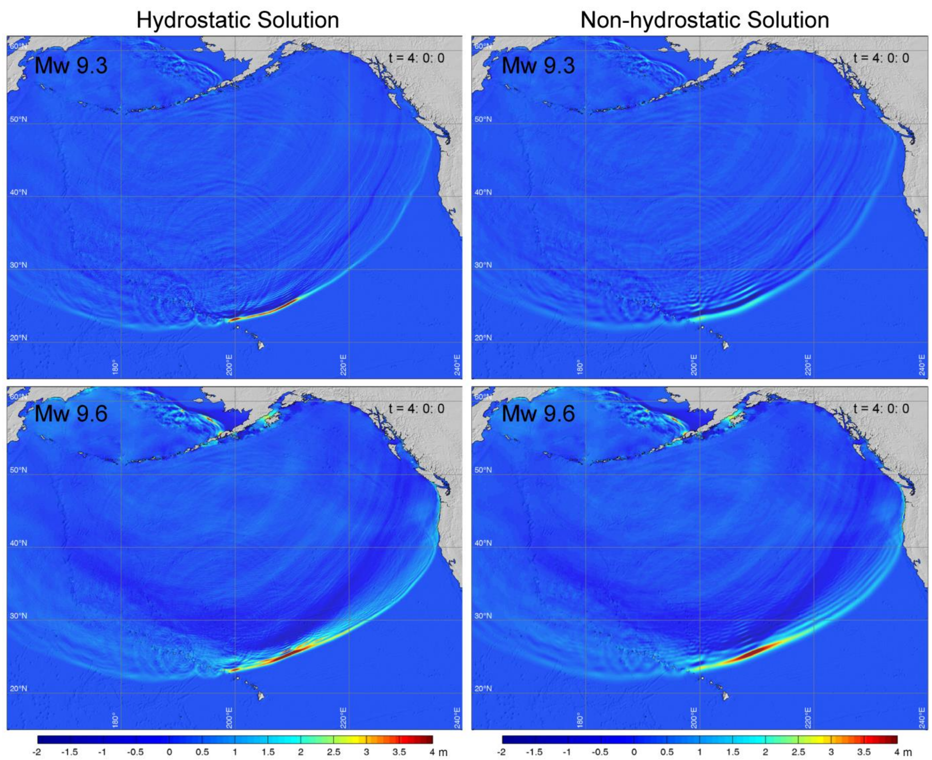

FIG. 7. Sea-surface elevations 4 hours after tsunami generation by Mw 9.3 and 9.6 Aleutian earthquakes from hydrostatic and nonhydrostatic modeling.

The hydrostatic and non-hydrostatic solutions, which are based on the same initial conditions, show appreciably difference in the leading crest. The maximum amplitude from the Mw 9.3 scenario in Fig. 8 provides an illustration of the dispersion processes and the subsequent impact to the Hawaiian Islands. Frequency dispersion decreases the wave amplitude most rapidly near the source as shorter-period components separated from the leading crest. Diffraction of the long-crested wave generated by the rupture spreads the energy to the east and west further reducing the amplitude across the ocean. The wave packet produces well-defined, standing edge wave patterns over the insular shelf with localized amplification from constructive interference. Without dispersion, the wave components align more closely with the leading crest resulting in overestimation of the wave amplitude by 30 to 60% across the ocean as well as a smoother amplitude envelope from reduced shelf oscillation around the islands. Both solutions, however, give comparable wave amplitude over the insular shelf within the 100-m depth contour. Even though the nonhydrostatic solution has a smaller leading crest and a lower shoaling gradient, the steep insular slope and shallow shelf appear to amplify energy from the wave packet. Without masking from an overestimated leading crest, the amplitude pattern along the island chain clearly resembles the inter-island and shelf modes (Figs. A1 and A2). The Mw 9.6 earthquake with uniform slip over a large rupture area generates a tsunami with longer periods and less dispersion. Fig. 9 shows closer predictions of the wave amplitude across the North Pacific with 10~30% difference between the hydrostatic and nonhydrostatic solutions. Since the insular shelves are less effective in trapping long-period waves, the nonhydrostatic approach produces consistently smaller wave amplitude near the shore. In comparison to the Mw 9.3 scenario, the longer waves result in greater impacts at Kahului, Maui (see Fig. 4b for location), which is susceptible to inter-island oscillations.

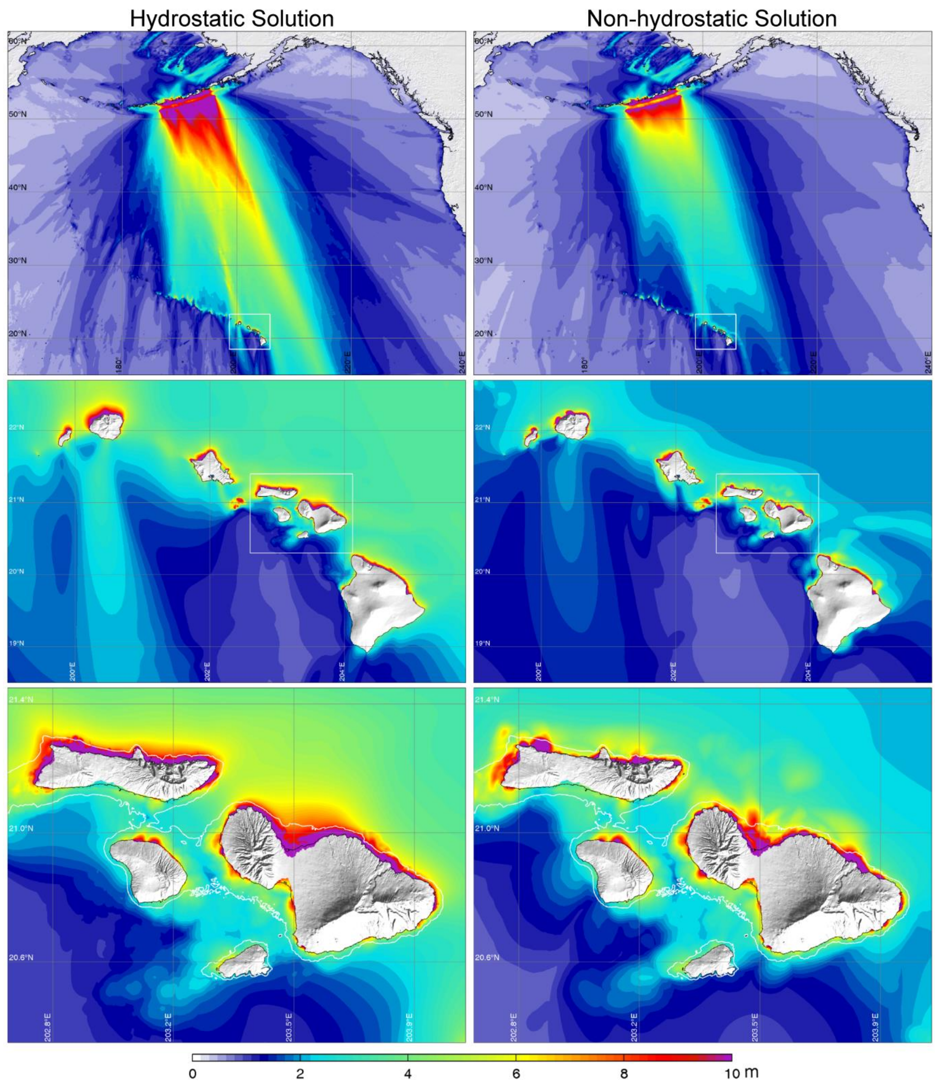

FIG. 8. Maximum sea-surface elevations of tsunamis generated by Mw 9.3 Aleutian earthquake from hydrostatic and nonhydrostatic modeling. White rectangles in top two rows delineate regions for close-up view in the panels immediately below and white lines in the bottom row are 100-m depth contours indicating the approximate extent of insular shelves.

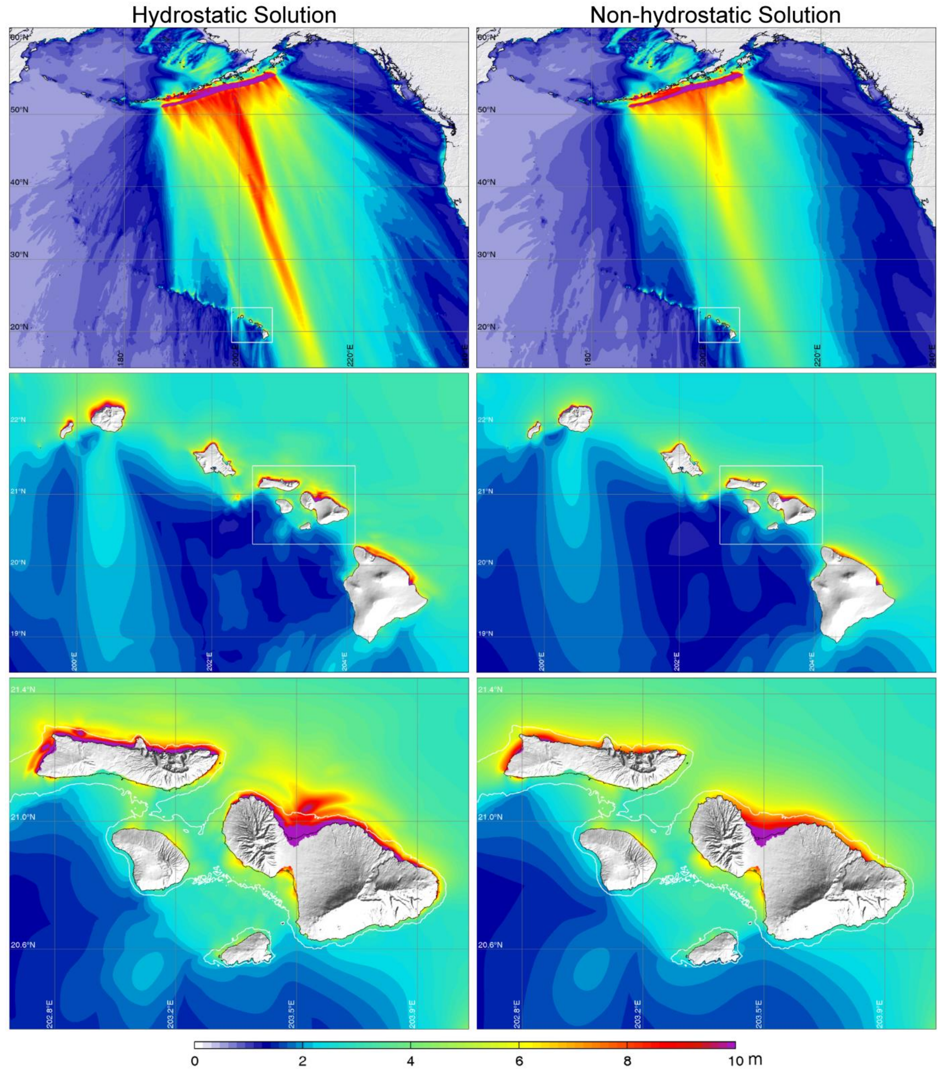

FIG. 9. Maximum sea-surface elevations of tsunamis generated by Mw 9.6 Aleutian earthquake from hydrostatic and nonhydrostatic modeling. White rectangles in top two rows delineate regions for close-up view in the panels immediately below and white lines in the bottom row are 100-m depth contours indicating the approximate extent of insular shelves.

B. Shelf and Near-shore Processes

The tsunamis generated by the Mw 9.3 and 9.6 Aleutian earthquakes have distinct dominant periods to excite selected ranges of oscillation modes along the Hawaiian Island chain. These include shelf oscillation modes from 11 to 30 min as well as inter-island standing waves from 33 to 75 min (Figs. A1 and A2). Trapping of incident wave energy occurs at the modal periods and the lack of well-defined nodal lines suggests formation of partial standing waves with energy leakage over time (Cheung et al., 2013). The processes lead to rapid buildup and gradual attenuation of coastal surges when a wave packet with coincidental periods passes through the islands. Superposition of standing edge waves from various oscillation modes very often creates large localized surge and runup several cycles after initial arrival (e.g., Roeber et al., 2010; Yamazaki and Cheung, 2011). This is in contrast to the leading crest, which typically has the largest amplitude across the open ocean, but does not necessarily produce the most severe impact at the shore. The hydrostatic and nonhydrostatic approaches provide different predictions of the initial wave packet (Figs. 5 and 6), which strongly influences the interisland, shelf, and near-shore processes in delineating inundation along the island chain.

Kauai and Niihau at the western end of the major Hawaiian Islands experience distinct wave dynamics due to their steep insular slopes and separation from the rest of the archipelago by a wide channel. The conditions favor shorter-period shelf modes with relatively weak interisland oscillations. Fig. 10 shows the difference in maximum surface elevations predicted by nonhydrostatic and hydrostatic modeling within the level-3 grid as well as a close-up view at Hanalei. Dispersion results in consistently smaller wave amplitude across the ocean, but trapping of the leading and trailing waves leads to larger surges over most the insular shelf for the Mw 9.3 event. This is most prominent off the north shore of Kauai, where the nonhydrostatic model gives significantly larger surges outside the shelf. The drawdown from recession of the initial flood wave driven by vertical inertia on the steep insular slope coincides with arrival of the deep trough and the subsequent upswing adds to the surge from the second peak in a local resonance process (Bai et al., 2018a). The floodwater covers the entire coastal and alluvial plain of Hanalei. The runup on headlands to the west reaches 41.1 m, which is one of the most severe around Kauai and is far larger than the observed 13.7 m in the same area from the most destructive, 1946 Aleutian tsunami (Walker, 2004). Despite having smaller nearshore surges, the hydrostatic model can still produce larger runup on steep terrain due to the lack of inertia in the vertical direction. The Mw 9.6 event has longer-period waves that become out of phase in the swash processes and are less susceptible to trapping on the shelf. The runup from the nonhydrostatic model reaches a lower value of 33.1 m at Hanalei. The hydrostatic solution tends to give larger surges along shorelines with gentler insular slopes and wider shelves due to the overestimated leading crest and shoaling gradient from the lack of dispersion.

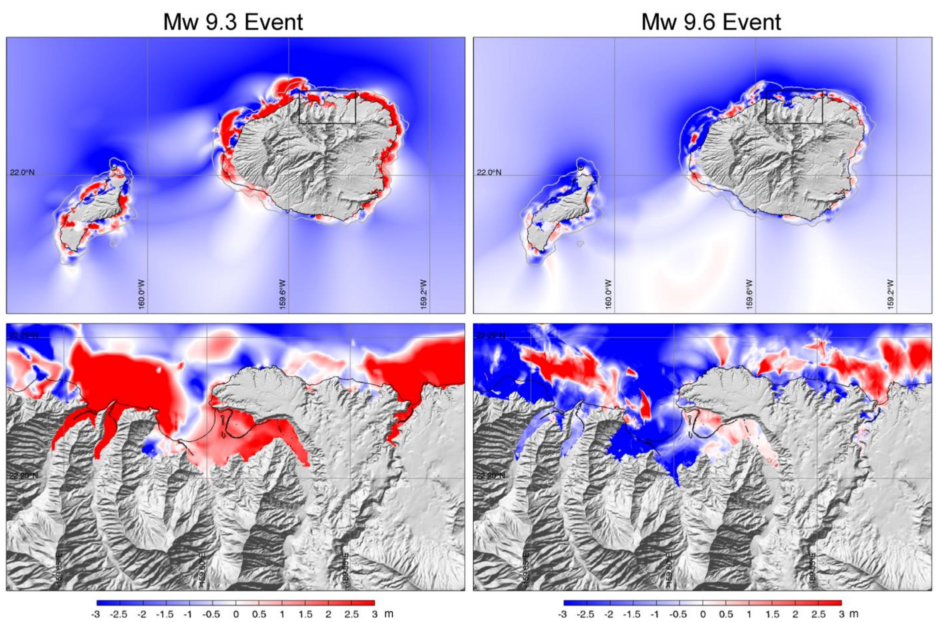

FIG. 10. Difference in maximum sea-surface elevations around Kauai and Hanalei for the Mw 9.3 and 9.6 events from hydrostatic and nonhydrostatic modeling with positive values indicating higher predictions from the latter and vice versa. Black rectangles in top panels delineate areas for close-up view in bottom panels. Black lines denote initial waterlines and grey lines are 100-m depth contours indicating the approximate extent of insular shelves.

The insular slope and shelf vary notably around Oahu with distinct modulations of the hydrostatic and nonhydrostatic processes in defining the maximum surface elevation as well as the difference between the two approaches. Fig. 11 shows the results from the level-3 Oahu and level-4 Haleiwa grids. Similar to the Mw 9.3 event on Kauai, the wave packet resonates over the steep insular slope off the west and north shores to produce greater surface elevation beyond the shelf in the nonhydrostatic solution. This is particularly evident in the close-up view at Haleiwa on the north shore, where larger flow depth extends well into river valleys and the runup reaches 29.2 m on the foothill. In the same area for comparison, the 1957 Aleutian tsunami produced the largest observed runup of 6.7 m among the five most destructive historical events (Walker, 2004). These swash processes become out-of-phase at the rest of island shores with gentler slopes, where the larger leading crest and higher shoaling gradient from the hydrostatic model lead to overestimation of the nearshore surges. The Mw 9.6 event has reduced shelf oscillations due to the longer-period excitation. The nonhydrostatic model still gives elongated patches of larger wave amplitude over gentle insular slopes due to stronger excitation of the interisland oscillation modes, which have antinodes extending beyond the shelf edge (Fig. A1a). Haleiwa has notably lower runup of 12.4 m due to the long-period excitation. The hydrostatic model produces more energetic surges over most of the insular shelf and trends to give disproportionate runup along shorelines with steep slopes. A notable example is Keana at northwest Oahu (see Fig. 3c for location), where the runup on the steep headland is overestimated by ~15 m in both the Mw 9.3 and 9.6 scenarios.

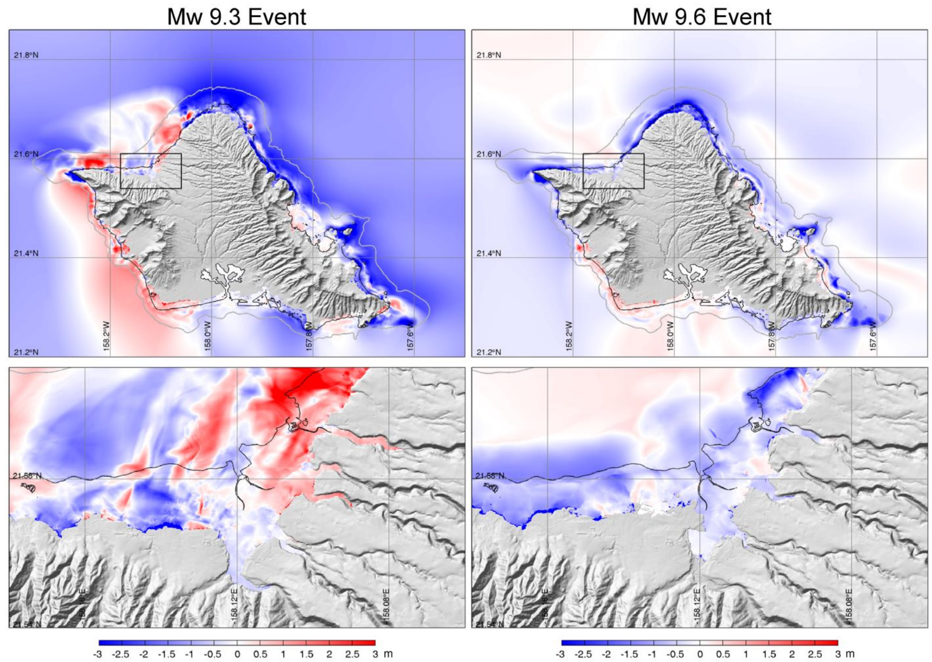

FIG. 11. Difference in maximum sea-surface elevations around Oahu and Haleiwa for the Mw 9.3 and 9.6 events from hydrostatic and nonhydrostatic modeling with positive values indicating higher predictions from the latter and vice versa. Black rectangles in top panels delineate areas for close-up view in bottom panels. Black lines denote initial waterlines and grey lines are 100-m depth contours indicating the approximate extent of insular shelves.

The interconnected insular slopes and shelves at Maui Nui host a number of short-period modes, which notably contribute to the larger, localized peak surface elevation in sheltered waters from nonhydrostatic modeling of the Mw 9.3 event, as shown in Fig. 12. Kahului Bay on the north side has a band of larger amplitude with runup reaching 23.5 m at the shore versus the largest observed value of 8.5 m from the 1946 Aleutian tsunami (Walker, 2004). The longer waves of the Mw 9.6 event are more effective in exciting the interisland modes, in which large antinodes are situated over the entire Maui Nui providing an explanation for the slightly larger amplitude over the gentle insular slope from the nonhydrostatic model. Hawaii Island has very narrow or no insular shelves, except for the northwest-facing shore and a segment outside Hilo Bay, where the nonhydrostatic model produces larger surges for the Mw 9.3 event as indicated in

Accepted to Phys. Fluids 10.1063/5.0152104

Fig. 13. The nearshore surge along the rest of island shores is mostly overestimated by the hydrostatic model. This includes Hilo Bay, where V-shape embayment appears to favor amplification of a larger leading crest, which produces 33.1 m of runup versus 27.8 m from the nonhydrostatic model. In comparison, observed runup from the 1946 Aleutian tsunami reaches 9.1 m in the same area (Walker, 2004). The nonhydrostatic model gives consistently lower surges around the island for the Mw 9.6 event, but slightly larger amplitude over steep offshore slopes, which are not influenced by the interisland oscillation modes. This is likely a result of local resonance of the wave packet that does not extend to the shore due to the lack of shallow shelves for energy trapping. The hydrostatic model consistently overestimates the runup on steep mountain slopes by a considerable margin, especially at Kalaupapa and Halawa, Molokai; Kahakuloa, Maui; and Wapio, Hawaii Island facing the incident waves from the north (See Figs. 4b and 4c for location).

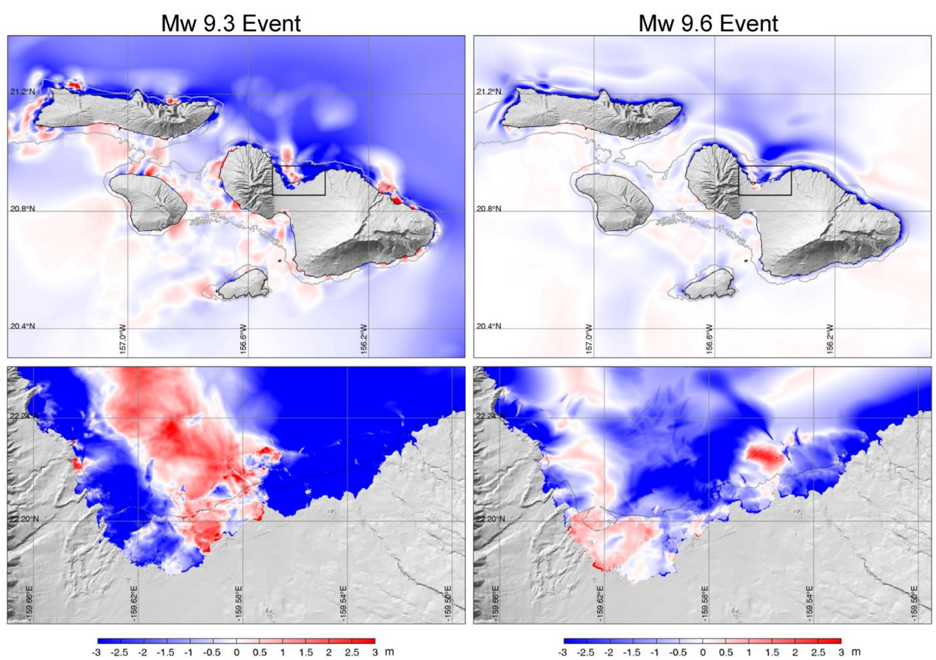

FIG. 12. Difference in maximum sea-surface elevations around Maui Nui and Kahului for the Mw 9.3 and 9.6 events from hydrostatic and nonhydrostatic modeling with positive values indicating higher predictions from the latter and vice versa. Black rectangles in top panels delineate areas for close-up view in bottom panels. Black lines denote initial waterlines and grey lines are 100-m depth contours indicating the approximate extent of insular shelves.

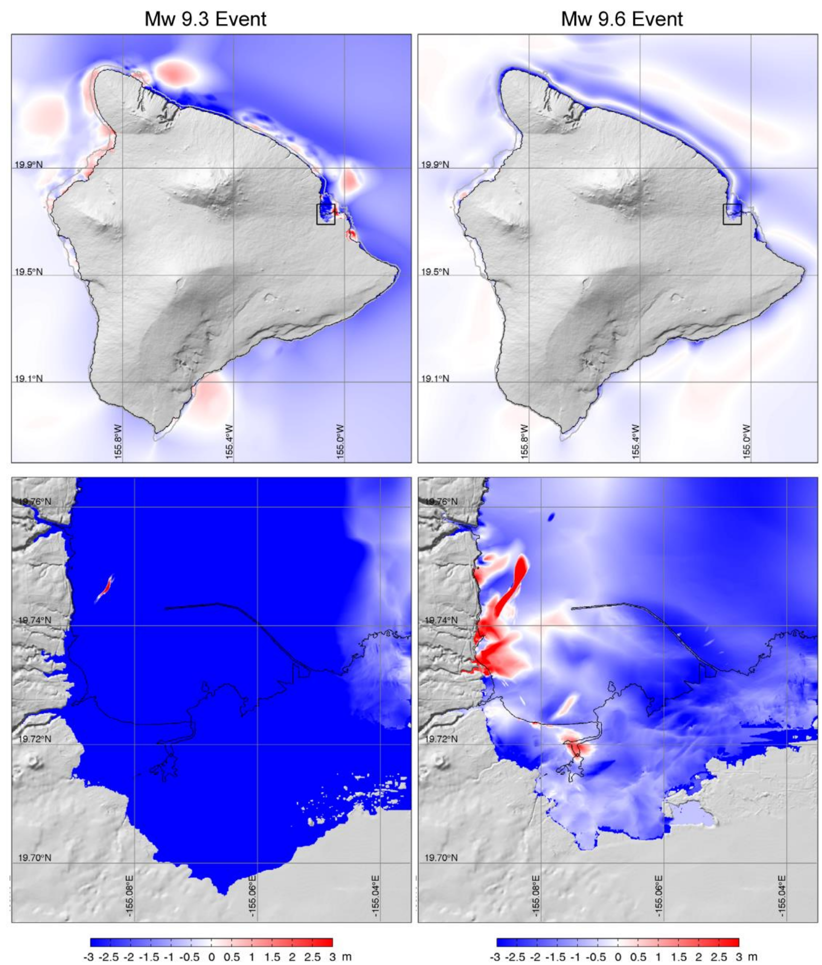

FIG. 13. Difference in maximum sea-surface elevations around Hawaii Island and Hilo for the Mw 9.3 and 9.6 events from hydrostatic and nonhydrostatic modeling with positive values indicating higher predictions from the latter and vice versa. Black rectangles in top panels delineate areas for close-up view in bottom panels. Black lines denote initial waterlines and grey lines are 100-m depth contours indicating the approximate extent of insular shelves.

C. Flow Depth, Runup, and Inundation

The primary concern for emergency management and engineering design is whether a numerical model misrepresents the impacts of tsunami events. This is also a scientific question for studies of tsunami physics and source mechanisms that rely primarily on numerical modeling. The comparisons from Figs. 10 to 13 have illustrated complex insular slope and shelf processes driven by the waveform and dominant period, which influence inundation predictions from hydrostatic and nonhydrostatic modeling. A larger leading crest due to the lack of dispersion does not necessary produce more severe coastal impacts, while a wave packet with the same energy can generate more severe shelf oscillations in comparison. The most striking is that nonhydrostatic effects can be prominent for tsunamis generated by a large Mw 9.3 earthquake raising questions on commonly-used, nonlinear shallow-water models in scientific research and engineering applications. The comprehensive inundation dataset covering 1330 km of Hawaii shorelines from hydrostatic and nonhydrostatic modeling allows a systematic analysis of the competing processes in defining the maximum flow depth, runup, and inundation. Since both approaches utilize a shock-capturing scheme for bores and hydraulic jumps, mass conservation across flow discontinuities is not an issue in the near-shore model results. Any discrepancies in the predictions can be attributed to the absence or presence of vertical flow dynamics in the model formulation.

The Mw 9.3 Aleutian earthquake with concentrated near-trench slip produces a tsunami, which cover the short-period oscillation modes around Hawaii, resulting in greater difference between the hydrostatic and nonhydrostatic predictions over shallow shelves. Table 2 provides a tally of the peak flow depth, runup, and inundation obtained from the 56 high-resolution grids around the Hawaiian Islands. The nonhydrostatic approach produces larger flow depth and runup in 45% and 29% of the 56 grids with significant implication for infrastructure planning and design, in which nonlinear shallow-water models remain as the primarily tool. The percentage varies among the islands. The wide insular shelf of Oahu tends to resonate with a dispersive wave packet producing larger coastal surges and flow depths in 75% of the 15 grids, but only resulting in larger runup in 20% of the grids. The steep volcanic mountain slope is prone to overestimation of runup from the lack of vertical inertia. This is exemplified by the consistently higher runup on the steep mountain slope of Hawaii Island by the hydrostatic model. The peak flow depth and runup, which are influenced by local topography, serves as key parameters for engineering design (Chock, 2016). The inundation represents the flooded area to quantify the overall tsunami impact for emergency management. The nonhydrostatic model produces more severe inundation for 39% of the 56 grids that have relatively flat coastal and alluvial plains prone to flooding by rising surges. The percentage is higher for Kauai and Oahu at 67% and 60% due to resonance on the insular shelf and slope complex. Trapping of the dispersive wave packet over Maui Nui does not appear to produce more severe impact as the larger amplitude areas are primarily offshore over the shelf on the leeside (Fig. 12). The hydrostatic model overestimates the inundation in 94% of the grids for Hawaii Island, which does not have notable insular shelves, except for short segments of the northwest and northeast-facing shores. The inundation on the steep terrain is driven by runup enhanced by the lack of vertical inertia in the model.

TABLE 2. Comparison of hydrostatic (HY) and nonhydrostatic (NH) model results from the finest grid at level 4 or 5 for the tsunami generated by the Mw 9.3 Aleutian earthquake.

	# Grids	Larger Flow Depth		Larger Runup		Larger Inundation	
		HY	NH	HY	NH	HY	NH
Kauai	9	4	5	4	5	3	6
Oahu	15	4	11	12	3	6	9
Maui Nui	16	11	5	8	8	10	6
Hawaii	16	12	4	16	0	15	1
Statewide	56	31	25	40	16	34	22

TABLE 3. Comparison of hydrostatic (HY) and nonhydrostatic (NH) model results from the finest grid at level 4 or 5 for the tsunami generated by the Mw 9.6 Aleutian earthquake.

	# Grids	Larger Flow Depth		Larger Runup		Larger Inundation	
		HY	NH	HY	NH	HY	NH
Kauai	9	5	4	7	2	8	1
Oahu	15	13	2	13	2	13	2
Maui Nui	16	12	4	13	3	14	2
Hawaii	16	14	2	15	1	16	0

Statewide	56	44	12	48	8	51	5

The tsunami generated by the Mw 9.6 Aleutian earthquake has longer periods due to the uniform slip over a much larger rupture area and excites primarily the interisland oscillation modes with lesser contributions from short-period trailing waves. Table 3 provides a tally of the model results from the 56 high-resolution grids around the Hawaiian Islands. Wave dispersion is still a notable process in trans-oceanic propagation, but the vertical flow inertia has reduced effect at the shore. The larger leading crest from the hydrostatic model results in overestimated flow depth, runup, and inundation in 79, 86, and 91% of the 56 grids. The percentages are even higher for Hawaii Island with steep insular slopes and very narrow to no insular shelves. The results are mostly consistent among the islands, except for the flow depth of Kauai, where the insular shelf is still effective in trapping the short-period trailing waves (Fig. 10). In comparison, the hydrostatic model overestimates the flow depth, runup, and inundation for 55, 71, and 61% of the grids under the more dynamic Mw 9.3 event. This has significant implication for the use of hydrostatic modeling to infer source parameters of megathrust earthquakes, as the overestimated wave amplitude and runup will inevitably lead to underestimation of the slip or vice versa in matching available tsunami measurements. The tendency for more conservative impact predictions at some shorelines is not necessarily receptive to emergency management either, especially for such extreme events involving evacuation of a significant portion of the population. After an extensive review by an advisory panel from the scientific and engineering communities, the state of Hawaii proceeded with the nonhydrostatic model results for the development of tsunami inundation maps.

The intercomparison reveals added values in nonhydrostatic modeling and supports the use of its data products for emergency management in Hawaii. The Mw 9.3 earthquake produces a tsunami with more focused energy that dominates the inundation along 90% of the shorelines. The longer waves of the Mw 9.6 event produce greater impacts in areas susceptible to inter-island oscillations, such as Kahului, Maui (Figs. 8 and 9). The computed runup is approximately three to four times higher than the largest historical observations around the islands. Aggregation of the model results from the two scenarios provided a set of tsunami inundation maps for infrequent and high-impact events to supplement the long-standing approach based on the five most destructive tsunamis in the last 200 years. Three of the four Hawaii counties have already implemented, and one is in the process of developing, two-tier evacuation maps to systematically account for extreme and more frequent tsunami events. The Pacific Tsunami Warning Center modified its operating procedures and data products for two levels of tsunami warnings. This had been a significant change to the emergency management procedures in Hawaii since implementation of tsunami evacuation maps in 1961 and is necessary for a state with a large population residing in coastal and alluvial plains bordering steep mountain slopes. For example, the most populated Oahu has 9% and 35% of its residents in the first and second-tier evacuation zones (based on 2014 population data). The sheer number of evacuees posts a logistic problem for tsunamis arriving in 4.5 hours after the earthquake. The two-tier evacuation, which strikes a balance between logistics, public safety, and economic cost, provides an effective measure to manage and mitigate tsunami hazards in Hawaii.

V. CONCLUSIONS AND RECOMMENDATIONS

Recent advances in nonhydrostatic modeling have improved understanding of tsunami physics and the capabilities to describe higher-order processes beyond the shallow-water range. The extension of Hawaii's tsunami inundation maps from historical-based to include extreme Mw 9.3 and 9.6 Aleutian scenarios provided a timely use case for the emerging techniques a decade ago. A careful reexamination of the model results shows nonhydrostatic effects play a more prominent role than what is typically reported in the technical literature. The most commonly-related attribute is frequency dispersion, which reduces the leading crest amplitude to form a wave packet. This is in fact an important process for tsunami propagation even for the massive Mw 9.3 and 9.6 Aleutian events. However, a wave packet is prone to trapping by insular and continental shelves and the resulting resonance can produce greater coastal surges than a large leading crest with the same energy from hydrostatic modeling. A related higher-order property is the improvement in wave transformation over continental or insular slopes. The shoaling gradient decreases quadratically with the depth parameter versus a constant value in the hydrostatic approach that overestimates amplitude of short-period waves at the shore. Although not addressed in this study, the nonhydrostatic terms can describe tsunami generation from seafloor deformation over finite rise time for multiple ruptures lasting several minutes (e.g., Yamazaki et al., 2011; Bai et al., 2023).

A lesser discussed aspect in nonhydrostatic modeling is the vertical flow inertia, which can influence tsunami source and coastal runup processes. The inertia from a descending initial pulse can enhance the trough that follows an attenuating leading crest. The trough depth remains relatively uniform across the ocean and can exceed the leading crest amplitude in the far field. This is evident in the Mw 9.3 event modeled by the nonhydrostatic approach as well as recorded tide gauge data from destructive Aleutian tsunamis in Hawaii. Local resonance of a wave packet can occur over steep insular slopes of Hawaii. The deep trough may augment inertia-driven drawdown to produce a stronger upswing of the water surface that coincides with an arriving crest to amplify the surge on to the shore. Although the nonhydrostatic approach may produce larger flow depth at the shore and more severe inundation on flat coastal plains, the computed runup on steep mountain slopes tends to be smaller compared to the hydrostatic approach due to inclusion of the vertical flow inertia. The large volume of model data from the mapping project shows the hydrostatic approach does not necessarily produce more conservative assessment of tsunami impacts just because of overestimating the incident wave amplitude. Although the intercomparison is performed for the tropical volcanic island environment of Hawaii, the findings also have implications for impacts of far-field tsunamis at continental shores. A nonhydrostatic model, which accounts for higher-order tsunami processes in sufficient detail, is a preferred tool for hazard mapping, engineering design, and scientific research.

APPENDIX

The waters around the Hawaiian Islands are prone to long-period oscillations from tsunamis. Spectral analysis of the sea-surface elevation computed for the 2011 Tohoku tsunami reveals a series of interisland and shelf oscillation modes with periods from 11 to 75 min (Cheung et al., 2013). Fig. A1 provides representative oscillation modes along the major Hawaiian Islands and over the interconnected shelves and slopes of Maui Nui. The interisland standing waves extend 2400 km from Hawaii Island to Midway with strong amplification over Maui Nui, which transitions to elaborate inter-shelf oscillations with decreasing period. The oscillation modes for Kauai, Oahu, and Hawaii Island in Fig. A2 show a combination of high and low-energy standing edge waves over the respective insular shelves and slopes. The two systems of edge waves are coupled to have the same period despite their vastly different spatial scales. Oscillations with periods 10 min or less belong to the reef modes, which have strong influences on separation-driven near-shore currents, but have secondary signals at the sea surface. The oscillation modes are applicable to other events, as resonance of water waves is primarily a function of the bathymetry, and thus form the basis for inter-comparison and interpretation of the hydrostatic and nonhydrostatic model results presented in this paper.

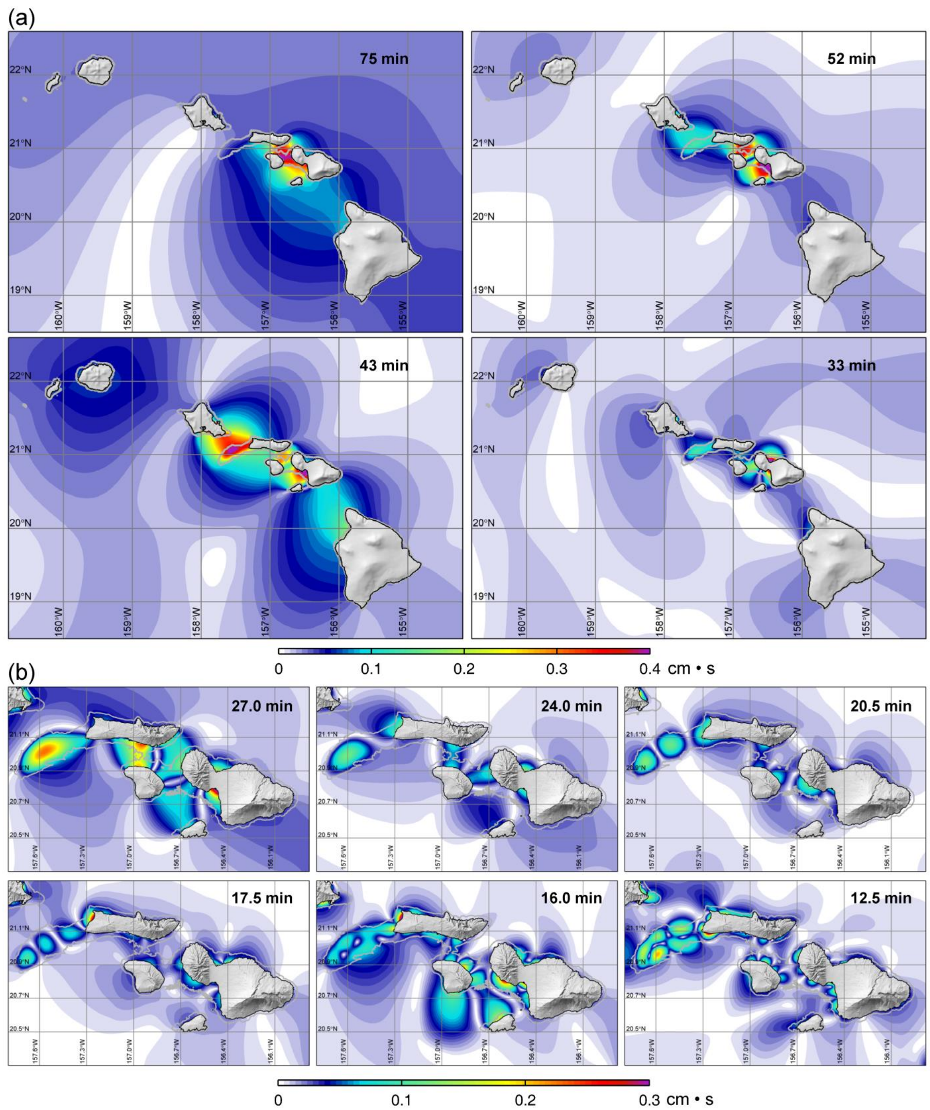

FIG. A1. Interisland and inter-shelf oscillation modes computed for the 2011 Tohoku tsunami [adapted from Cheung et al. (2013)]. (a) Hawaiian Islands. (b) Maui Nui. Grey lines are 100-m depth contours indicating the approximate extent of insular shelves.

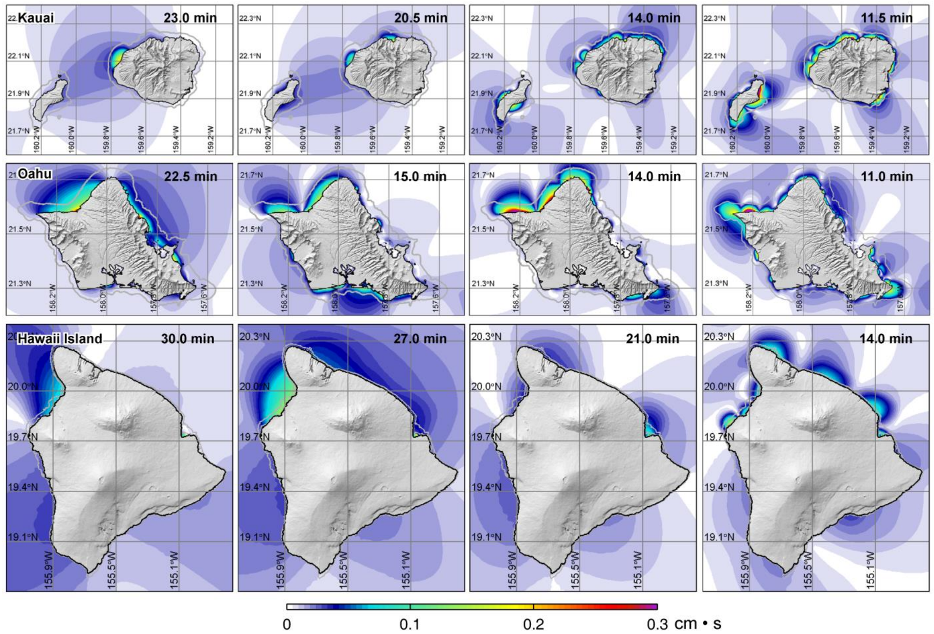

FIG. A2. Shelf and slope oscillation modes computed for the 2011 Tohoku tsunami around Kauai, Oahu, and Hawaii Islands [adapted from Cheung et al. (2013)]. Grey lines are 100-m depth contours indicating the approximate extent of insular shelves.

ACKNOWLEGEMENTS

The US National Tsunami Hazard Mitigation Program funded the tsunami inundation mapping project at the University of Hawaii through NA09NWS4670016 via a memorandum of agreement with Hawaii Emergency Management Agency. Rhett Butler developed and supplied the Aleutian earthquake sources under a separate contract. We thank the Hawaii State Earthquake and Tsunami Advisory Committee for the input to the inundation mapping effort as well as Thorne Lay and the four anonymous reviewers for their comments and suggestions on this paper. SOEST Contribution No. 11658.

AUTHOR DECALARATIONS

Conflict of Interest

The authors have no conflicts of interest to disclose.

Author Contributions

Yefei Bai: Methodology (equal), Software (equal), Data curation (lead), Formal analysis (lead); Writing - review & editing (equal). **Yoshiki Yamazaki:** Methodology (equal), Software (lead), Data curation (equal), Formal analysis (equal); Writing - review & editing (equal). **Kwok Fai Cheung:** Conceptualization (lead); Funding acquisition (lead); Writing - original draft (lead), review & editing (lead); Formal analysis (equal).

DATA AVAILABILITY

The data that support the findings of this study are available from the corresponding authors upon reasonable request.

REFERENCES

Ammon, C.J., Ji, C., Thio, H.-K., Robinson, D., Ni, S., Hjorleifsdottir, V., Kanamori, H., Lay, T., Das, S., Helmberger, D., Ichinose, G., Polet, J., and Wald, D., "Rupture process of the 2004 Sumatra-Andaman earthquake," Science **308**(5725), 1133-1139 (2005).

Aránguiz, R., Shibayama, T., and Yamazaki, Y., "Tsunamis from the Arica-Tocopilla source region and their effects on ports of Central Chile," Nat. Haz., **71**(1), 175-202.

Baba, T., Allgeyer, S., Hossen, J., Cummins, P.R., Tsushima, H., Imai, K., Yamashita, K., and Kato, T., "Accurate numerical simulation of the far-field tsunami caused by the 2011 Tohoku earthquake, including the effects of Boussinesq dispersion, seawater density stratification, elastic loading, and gravitational potential change," Ocean Modell., **111**, 46–54, (2017).

Bai, Y. and Cheung, K.F., "Hydrostatic versus non-hydrostatic modeling of tsunamis with implications for insular shelf and reef environment," Coast. Eng. **117**, 32-43 (2016).

Bai, Y., Liu, C., Lay, T., Cheung, K.F., and Yamazaki, Y., "Fast and slow intraplate ruptures during the 19 October 2020 magnitude 7.6 Shumagin earthquake," Nat. Comm. **14**, 2015 (2023).

Bai, Y., Liu, C., Lay, T., Cheung, K.F., and Ye, L., “Optimizing a model of coseismic rupture for the 22 July 2022 Mw 7.8 Simeonof earthquake by exploiting acute sensitivity of tsunami excitation across the shelf break,” J. Geophys. Res. Solid Earth **127**(7), e2022JB024484 (2022).

Bai, Y., Yamazaki, Y., and Cheung, K.F., “Amplification of drawdown and runup over Hawaii's insular shelves by tsunami N-waves from mega Aleutian earthquake.” Ocean Modell. **124**, 61-74 (2018a).

Bai, Y., Yamazaki, Y., and Cheung, K.F., “Convergence of multilayer nonhydrostatic models in relation to Boussinesq-type equations,” J. Waterw. Port Coast. Ocean Eng. **144**(2), 06018001 (2018b).

Bai, Y., Yamazaki, Y., and Cheung, K.F. “NEOWAVE.” Proc. and Results of the 2015 National Tsunami Hazard Mitigation Program Model Benchmarking Workshop, Portland, Oregon, pp. 165-177 (2015).

Berryman, K., Wallace, L., Hayes, G., Bird, P., Wang, K., Basili, R., Lay, T., Pagani, M., Stein, R., Sagiya, T., Rubin, C., Barreintos, S., Kreemer, C., Litchfield, N., Stirling, M., Gledhill, K., Costa, C., The GEM Faulted Earth Subduction Characterization Project. Version 2.0, available from http://www.nexus.globalquakemodel.org/gem-faulted-earth/posts (2015).

Bletery, Q., Sladen, A., Delouis, B., Vallée, M. Nocquet, J.-M., Rolland, L., and Jiang, J., “A detailed source model for the Mw 9.0 Tohoku-Oki earthquake reconciling geodesy, seismology, and tsunami records,” J. Geophys. Res. Solid Earth **119**(10), 7936-7653 (2014).

Brooks, B.A., Goldberg, D., DeSanto, J., Ericksen, T.L., Webb, S., Mooner, S.L., Chadwell, C.D., Foster, J., Minson, S., Witter, R., Haeussler, P., Freymueller, J., Barnhart, W., Newitt, J., “Rapid shallow megathrust afterslip from the 2021 M8.2 Chignik Alaska earthquake revealed by seafloor geodesy,” Sci. Adv. **9**(17), eadf9299 (2023).

Butler, R., “Re-examination of the potential for great earthquakes along the Aleutian island Arc with implications for tsunamis in Hawaii,” Seimol. Res. Lett. **83**(1), 29-38 (2012).

Butler, R., Burney, D., Walsh, D., “Paleotsunami evidence on Kauai and numerical modeling of a great Aleutian tsunami,” Geophys. Res. Lett. **41**(19), 6795-6802 (2014).

Castro-Orgaz, O., Hager, W.H., and Katopodes, N.D., “Variational models for nonhydrostatic free-surface flow: A unified outlook to maritime and open-channel hydraulics development,” J. Hydraul. Eng. **149**(7), 04023014 (2023).

Casulli, V., and Stelling, G., “Numerical simulation of 3D quasi-hydrostatic, free surface flows,” J. Hydraul. Eng. **124**(7), 678-686 (1998).

Catalán, P.A., Aránguiz, R., González, G., Tomita, T., Cienfuegos, R., González, J., Shrivastava, M.N., Kumagai, K., Mokrani, C., Cortés, P. and Gubler, A., “The 1 April 2014 Pisagua tsunami: observations and modeling,” Geophys. Res. Lett. **42**(8), 2918-2925 (2015).

Cheung, K.F., Bai, Y., and Yamazaki, Y., “Surges around the Hawaiian Islands from the 2011 Tohoku tsunami,” J. Geophys. Res. Oceans **118**(10), 5703–5719 (2013).

Chock, G.Y.K., “Design for tsunami loads and effects in the ASCE 7-16 standard,” J. Struct. Eng. **142**(11), 04016093 (2016).

Cox, D.C., Potential Tsunami Inundation Areas in Hawaii, Report No. 14, Hawaii Institute of Geophysics, University of Hawaii, Honolulu, (1961).

Fletcher, C.H. and Sherman, C., “Submerged shorelines on Oahu Hawaii: archive of episodic transgression during the deglaciation,” J. Coast. Res. **17**(SI), 141–152 (1995).

Fraser, G.D., Eaton, J.P., and Wentworth, C.K., “The tsunami of March 9, 1957, on the Island of Hawaii,” Bull. Seismol. Soc. Am. **49**(1), 79-90 (1959).

Fujiwara, T., Kodaira, S., No, T., Kaiho, Y., Takahashi, N., and Kaneda, Y., “The 2011 Tohoku-Oki earthquake: Displacement reaching the trench axis,” Science **334**(6060), 1240 (2011).

Gica, E., Spillane, M., Titov, V., Chamberlin, C., and Newman, J., Development of the Forecast Propagation Database for NOAA’s Short Term Inundation Forecast for Tsunamis (SIFT). NOAA Technical Memorandum OAR PMEL-139, Pacific Marine Environmental Laboratory Seattle, WA (2008).

Green, C.K., "Seismic sea wave of April 1, 1946, as recorded on tide gauges," Eos Trans. Am. Geophys. Union **27**(4), 490-500 (1946).

Horrillo, J., Kowalik, Z., and Shigihara, Y., "Wave dispersion study in the Indian Ocean Tsunami of December 26, 2004," Mar. Geod. **29**(3), 149–166 (2006).

Huo, Z. and Liu, H., "Experimental study of the surge- and bore-induced impact pressure on a vertical wall and its foundation," Phys. Fluids **35**(1), 016602 (2023).

Imamura, F., Shuto, N., and Goto. C., "Numerical simulations of the transoceanic propagation of tsunamis," Proc. 6th Congress of the Asian and Pacific Regional Division, Int. Assoc. Hydraul. Res., Kyoto, Japan (1988).

Kanamori, H., "Mechanism of tsunami earthquakes," Phys. Earth Planet. Inter. **6**(5), 346-359 (1972).

Jeschke, A., Pedersen, G.K., Vater, S., and Behrens, J., "Depth-averaged non-hydrostatic extension for shallow water equations with quadratic vertical pressure profile: equivalence to Boussinesq-type equations," Int. J. Numer. Meth. Fluids **84**(10), 569-583 (2017).

Kirby, J.T., Shi, F., Tehranirad, B., Harris, J.C., and Grilli, S.T., "Dispersive tsunami waves in the ocean: model equations and sensitivity to dispersion and Coriolis effects," Ocean Modell. **62**, 39–55 (2013).

Kowalik, Z. and Murty, T.S., "Numerical simulation of two-dimensional tsunami runup," Mar. Geod. **16**(2) 87-100 (1993).

La Selle, S., Richmond, B.M., Jaffe, B.E., Nelson, A.R., Griswold, F.R., Arcos, M.E.M., Chage, C., Bishop, J.M., Bellanova, P., Kane, H.H., Lunghino, B.D., and Gelfenbaum, G., "Sedimentary evidence of prehistoric distant-source tsunamis in the Hawaiian Islands," Sedimentology **67**(3), 1249-1273 (2020).

Lay, T. "A review of the rupture characteristics of the 2011 Tohoku-oki M_W 9.1 earthquake," Tectonophysics **733**, 4-36 (2018).

Lay, T., Kanamori, H., Ammon, C.J., Nettles, M., Ward, S.N., Aster, R.C., Beck, S.L., Bilek, S.L., Brudzinski, M.R., Butler, R., DeShon, H.R., Ekstrom, G., Satake, K., Sipkin, S., "The great Sumatra-Andaman earthquake of 26 December 2004," Science **308**(5725), 1127-1133 (2005).

Lay, T., Ye, L., Kanamori, H., Yamazaki, Y., Cheung, K.F., Kwong, K., and Koper, K.D., "The October 28, 2012 Mw 7.8 Haida Gwaii underthrusting earthquake and tsunami: Slip partitioning along the Queen Charlotte Fault transpressional plate boundary," Earth Planet. Sci. Lett. **375**, 57-70 (2013).

LeVeque, R.J., George, D.L., and Berger, M.J., "Tsunami modelling with adaptively refined finite volume methods," Acta Numerica **20**, 211-289 (2011).

Li, L. and Cheung, K.F., "Numerical dispersion in non-hydrostatic modeling of long-wave propagation," Ocean Modell. **138**, 68-87(2019).

Li, L., Cheung, K. F., Yue, H., Lay, T., and Bai, Y. "Effects of dispersion in tsunami Green's functions and implications for joint inversion with seismic and geodetic data: A case study of the 2010 Mentawai M_W 7.8 earthquake." Geophys. Res. Lett. **43**(21), 11,182-11,191 (2016).

Li, S., and Freymueller, J.T., "Spatial variation of slip behavior beneath the Alaska Peninsula along Alaska-Aleutian subduction zone," Geophys. Res. Lett. **45**(8), 3453-3460 (2018).

Liu, P.L.-F., Cho, Y.-S., Briggs, M.J., Kânoğlu, U., Synolakis, C.E., "Runup of solitary waves on a cicular island," J. Fluid Mech. **302**, 259-285 (1995).

Mader, C.L., Numerical Modeling of Water Waves. Second Edition, CRC Press, Baco Raton, Florida, 288 p (2004).

Madsen, P.A. and Sørensen, O.R., "A new form of Boussinesq equations with improved linear dispersion characteristics. Part 2: A slowly-varying bathymetry," Coast. Eng. **18**(3-4), 183-204 (1992).

Okada, Y., "Surface deformation due to shear and tensile faults in a half-space." Bull. Seismol. Soc. Am., **75**(4), 1135-1154 (1985).

Peregrine., D.H., "Long waves on a beach," J. Fluid Mech., **27**, 815-827 (1967).

Roeber, V., Yamazaki, Y., and Cheung, K.F., "Resonance and impact of the 2009 Samoa tsunami around Tutuila, American Samoa," Geophys. Res. Lett. **37**(21), L21604 (2010).

Roeber, V., and Cheung, K.F., "Boussinesq-type model for energetic breaking waves in fringing reef environments," Coast. Eng. **70**, 1-20 (2012).

Romano, F., Piatanesi, A., Lorito, S., D'Agostino, N., Hirata, K., Atzori, S., Yamazaki, Y., and Cocco, M., "Clues from joint inversion of tsunami and geodetic data of the 2011 Tohoku-oki earthquake," Sci. Rep. **2**, 385 (2012)

Saito, T., Inazu, D., Miyoshi, T., Hino, R., "Dispersion and nonlinear effects in the 2011 Tohoku-Oki earthquake tsunami," J. Geophys. Res. Oceans, **119**(8), 5160–5180 (2014).

Salazar, D., Easton, G., Goff, J., Guendon, J.L., González-Alfaro, J., Andrade, P., Villagrán, X., Fuentes, M., León, T., Abad, M. and Izquierdo, T., "Did a 3800-year-old Mw ~9.5 earthquake trigger major social disruption in the Atacama Desert?" Sci. Adv. **8**(14), eabm2996 (2022).

Stelling, G.S., and Duinmeijer, S.P.A., "A staggered conservative scheme for every Froude number in rapidly varied shallow water flows," Int. J. Numer. Meth. Fluids **43**(12), 1329-1354 (2003).

Stelling, G.S., and Zijlema, M., "An accurate and efficient finite-difference algorithm for non-hydrostatic free-surface flow with application to wave propagation," Int. J. Numer. Meth. Fluids **43**(1), 1-23 (2003).

Titov, V.V. and Synolakis, C.E., "Numerical modeling of tidal wave runup," J. Waterw. Port Coast. Ocean Eng. **124**(4), 157–171 (1998).

Walker, D., "Regional Tsunami evacuations for the state of Hawai`i: a feasibility study on historical runup data," Sci. Tsunami Haz. **22**(1), 3-22 (2004).

Wei, Y., Mao, X.Z., and Cheung, K.F., "Well-balanced finite-volume model for long-wave runup," J. Waterw. Port Coast. Ocean Eng. **132**(2), 114-124 (2006).

Witter, R.C., Carver, G.A., Briggs, R.W., Gelfenbaum, G., Koehler, R.D., La Selle, S.P., Bender, A.M., Engelhart, S.E., Hemphill-Haley, E., Hill, T.D., "Unusually large tsunamis frequent a currently creeping part of the Aleutian megathrust," Geophys. Res. Lett. **43**(1), 76-84 (2016).

Witter, R.C., Briggs, R.W., Engelhalt, S.E., Gelfenbaum, G., Koehler, R.D., Nelson, A.R., and Wallace, K.L., "Evidence for frequent, large tsunamis spanning locked and creeping parts of the Aleutian megathrust," Geo. Soc. Am. Bull. **131**(5-6), 707-729 (2018).

Yamazaki, Y, Bai, Y., Goo, L.L., Cheung, K.F., and Lay, T., "Nonhydrostatic modeling of tsunamis from earthquake rupture to coastal impact," J. Hydraul. Eng. **149**, in press (2023).

Yamazaki, Y. and Cheung, K.F., "Shelf resonance and impact of near-field tsunami generated by the 2010 Chile earthquake," Geophys. Res. Lett. **38**(12), L12605 (2011).

Yamazaki, Y., Cheung, K.F., and Kowalik, Z., "Depth-integrated, non-hydrostatic model with grid-nesting for tsunami generation, propagation and run-up," Int. J. Numer. Meth. Fluids **67**(12), 2081-2107 (2011).

Yamazaki, Y., Cheung, K.F., Kowalik, Z., Lay, T., and Pawlak, G. "NEOWAVE." Proc. and Results of the NTHMP Model Benchmarking Workshop, NOAA Special Report, Galveston, Texas, pp. 239-302 (2012).

Yamazaki, Y., Cheung, K.F., and Lay, T., "A self-consistent fault slip model for the 2011 Tohoku earthquake and tsunami," J. Geophys. Res. Solid Earth **123**(2), 1435-1458 (2018).

Yamazaki, Y., Cheung, K.F., and Lay, T., "Modeling of the 2011 Tohoku near-field tsunami from finite-fault inversion of seismic waves," Bull. Seismol. Soc. Am. **103**(2B), 1444-1455. (2013).

Yamazaki, Y., Kowalik, Z., and Cheung, K.F., "Depth-integrated, non-hydrostatic model for wave breaking and run-up," Int. J. Numer. Meth. Fluids **61**(5), 473-497 (2009).

Yamazaki, Y., Lay, T., and Cheung, K. F., "A compound faulting model for the 1975 Kalapana, Hawaii, earthquake, landslide and tsunami," J. Geophys. Res. Solid Earth **126**(11), e2021JB022488 (2021).

Ye, L., Bai, Y., Si, D., Lay, T., Cheung, K.F., and Kanamori, H., "Rupture model for the 29 July 2021 Mw 8.2 Chignik, Alaska earthquake constrained by seismic, geodetic, and tsunami observations," J. Geophys. Res. Solid Earth **127**(7), e2021JB023676 (2022).

Accepted to Phys. Fluids 10.1063/5.0152104

Yue, H., Lay, T., Li, L., Yamazaki, Y., Cheung, K. F., Rivera, L., Hill, E. M., Sieh, K., Kongko, W., and Muhari, A., "Validation of linearity assumptions for using tsunami waveforms in joint inversion of kinematic rupture models: Application to the 2010 Mentawai M_w 7.8 tsunami earthquake," J. Geophys. Res. Solid Earth **120**(3), 1728-1747 (2015).